Numerical studies on the instantaneous fluid–structure interaction of an air-inflated flexible membrane in turbulent flow

Guillaume de Nayer, Andreas Apostolatos, Jens Nikolas Wood, Kai-Uwe Bletzinger, Roland Wüchner, Michael Breuer

Journal of Fluids and Structures 82 (2018) 577–609

Contents lists available at ScienceDirect

Journal of Fluids and Structures

journal homepage: www.elsevier.com/locate/jfs

Numerical studies on the instantaneous fluid–structure interaction of an air-inflated flexible membrane in turbulent flow

G. De Nayer [a], A. Apostolatos [b], J.N. Wood [a], K.U. Bletzinger [b], R. Wüchner [b], M. Breuer [a,*]

[a] Professur für Strömungsmechanik, Helmut-Schmidt-Universität Hamburg, D-22043 Hamburg, Germany
[b] Lehrstuhl für Statik, Technische Universität München, D-80290 München, Germany

ARTICLE INFO

Article history:
Received 24 March 2018
Received in revised form 5 June 2018
Accepted 16 August 2018

Keywords:
Fluid–structure interaction (FSI)
Hemisphere
Membrane
Turbulent flow
Large-eddy simulation (LES)
Inflow generator

ABSTRACT

The present paper is the numerical counterpart of a recently published experimental investigation by Wood et al. (2018). Both studies aim at the investigation of instantaneous fluid–structure interaction (FSI) phenomena observed for an air-inflated flexible membrane exposed to a turbulent boundary layer, but looking at the coupled system based on different methodologies. The objective of the numerical studies is to supplement the experimental investigations by additional insights, which were impossible to achieve in the experiments. Relying on the large-eddy simulation technique for the predictions of the turbulent flow, non-linear membrane elements for the structure and a partitioned algorithm for the FSI coupling, three cases with different Reynolds numbers (Re = 50,000, 75,000 and 100,000) are simulated. The time-averaged first and second-order moments of the flow are presented as well as the time-averaged deformations and standard deviations. The predictions are compared with the experimental references data solely available for 2D planes. In order to better comprehend the three-dimensionality of the problem, the data analysis of the predictions is extended to 3D time-averaged flow and structure data. Despite minor discrepancies an overall satisfying agreement concerning the time-averaged data is reached between experimental data in the symmetry plane and the simulations. Thus for an in-depth analysis, the numerical results are used to characterize the transient FSI phenomena of the present cases either related to the flow or to the structure. Particular attention is paid to depict the different vortex shedding types occurring at the top, on the side and in the wake of the flexible hemispherical membrane. Since the fluid flow plays a significant role in the FSI phenomena, but at the same the flexible membrane with its eigenmodes also impacts the deformations, the analysis is based on the frequencies and Strouhal numbers found allowing to categorize the different observations accordingly.

1. Introduction

Light-weight thin-walled membranous structures are common in modern civil engineering and design. They are flexible, transportable and fast and easy to shape due to the non-existence of bending stiffness. To induce a form and to maintain a tensile state, a pre-stress has to be applied. Two major types of pre-stresses can be pointed out: The mechanically induced

* Corresponding author.
E-mail address: breuer@hsu-hh.de (M. Breuer).

https://doi.org/10.1016/j.jfluidstructs.2018.08.005

tension by specific boundary conditions and the pre-stress due to internal pressure. When the structure is exposed to a fluid flow and undergoes fluid–structure interactions (FSI), the pre-stress plays an important role in the stabilization of the whole construction. In order to optimize such buildings or avoid the damage of the material caused by FSI, experimental and numerical investigations are necessary. Wood et al. (2018) recently gave an overview on experimental FSI-related studies involving membranes with application in civil engineering and other aeroelastic phenomena. In the current work a brief literature survey concentrates on corresponding numerical FSI research investigations with pre-stressed membrane models.

Glück et al. (2001) carried out numerical FSI investigations on a real-life structure, i.e., a tent roof under constant turbulent wind load. The equilibrium shape of the pre-stressed membrane was obtained by a form-finding technique before starting the simulation. To solve the FSI problem, a partitioned approach based on an in-house finite-volume (FV) fluid code and a commercial finite-element (FE) program combined by the arbitrary Lagrangian–Eulerian (ALE) method was applied. The CFD code solved the unsteady Reynolds-averaged Navier–Stokes (URANS) equations combined with the classical k-ε turbulence model. The setup led to steady deformations. In Glück et al. (2003) the inflow conditions were modified to take a gust-like laminar inflow into account resulting in an unsteady behavior of the construction. In both studies pressure distributions and deformations of the FSI interface were presented. However, there was no discussion on the physics or comparison with experimental measurements. The cases were basically used to demonstrate the stability and the robustness of the FSI coupling scheme.

A complementary experimental and numerical investigation was conducted by Rank et al. (2003) on a big mobile membranous umbrella. A 1:50 model was put into a wind tunnel. The forces in the retention cables and the deformation of the thin structure were measured. For the simulation the same FSI environment as in Glück et al. (2001) was applied. Despite some discrepancies, the predicted deformed shape and the forces in the cables matched quite well with the experimental data.

Wüchner et al. (2007) presented two studies on real-life civil engineering constructions: A hanging roof and a four-point tent. The pre-stresses in the membranes were fixed and the respective equilibrium shapes were determined by separate form-finding procedures before the FSI simulations (Wüchner and Bletzinger, 2005). A gust-like wind load was imposed to mimic the time-dependence in the natural environment. A commercial FV fluid solver based on the URANS equations with the SST turbulence model and an in-house FE structure code were coupled. Weak and strong FSI schemes were successively taken into account. Both cases led to an unsteady behavior. However, as in the simulations mentioned above, no deep discussion on the physics or comparison with measurements were presented. Again, the goal was to test the FSI coupling schemes and to assess the computational FSI framework.

In Kupzok (2009) the same FSI code as used in Wüchner et al. (2007) was applied on the ARIES[1] structure. Different wind loads and directions were examined in steady-state computations. The effect of the wind on the back and front sides of the structure were discussed in detail. Additionally, transient simulations were carried out using gust-like inflow conditions. Studying the resulting deformations of the membrane, the author made recommendations to the designers to adjust the pre-stress of the membrane.

Hojjat et al. (2010) used a similar FSI framework and extended it to realize shape optimization in the context of wind engineering. Several optimization strategies were successfully tested on a light slender membranous roof exposed to a turbulent boundary layer. The equilibrium shape for a defined pre-stress distribution within the initial structure was determined by a form-finding computation. Then, for each specified state of the membranous construction, the problem was solved as a steady problem. After optimization a strong improvement of the objective function was observed. The final form and the pressure distribution on the FSI interface were presented.

Due to their low weight and costs, thin-walled membranes fit perfectly for temporary or emergency buildings. As an example the "uLites" research program[2] develops the technology to enable a fast assembly of light-weight structures with integrated solar cells. Wind-tunnel experiments were performed to estimate forces and deformations. In order to minimize the development costs, the numerical counterpart was carried out by Rossi (2013) based on an embedded and partitioned FSI approach using FE solvers. No data was published yet for comparison.

Recently, Michalski et al. (2011, 2015) carried out transient simulations on big umbrellas in turbulent wind flows. The applied commercial software environment was based on FE solvers and the ALE method. The turbulent flow was predicted by the large-eddy simulation (LES) technique. In both investigations particular attention was laid on a consistent structural modeling of the pre-stressed membrane subjected to wind flow, i.e., the proper inclusion of shape-finding techniques in the overall simulation approach besides the pure FSI analysis. Furthermore, the authors ensured to synthetically mimic an atmospheric boundary layer. Information about the flow, the forces and the structural deformations predicted by the simulations were provided. Moreover, in order to enable a comparison with experimental data, strain gauges and cameras were put in and around the umbrellas to measure forces and moments of the structures as well as their deformations. Overall a good agreement between simulations and measurements was achieved. That demonstrates the applicability of numerical methods in modern civil engineering applications. However, because of the real scale of the investigated test cases, no fully controlled flow conditions could be guaranteed and therefore comparisons with the numerical results are extremely difficult.

[1] http://www.tensinet.com/index.php/component/tensinet/?view=project{&}id=4171.

[2] http://www.cimne.com/websasp/ulites/default.asp.

(a) Tent (Gentofte, Denmark). (b) Petroleum Coke Bulk Storage (Pittsburg).

Fig. 1. Examples of flexible air-inflated hemispheres.[3,4]

As obvious from the brief literature survey above, numerical investigations on fluid–structure interactions with membranous structures have become more and more important. Nevertheless, complementary experimental and numerical studies describing the whole FSI problem (fluid flow with detailed inflow conditions, structural deformations and the unsteady behavior) are still rare. This is especially true for studies which try to get some insights into the coupling phenomena found for these types of applications. Therefore, in the present study a geometrically simple real-life configuration borrowed from the civil engineering area is selected to fill this gap: A wall-mounted air-inflated hemisphere (see Fig. 1) exposed to a thick turbulent boundary layer. Preliminary experimental and numerical investigations related to the rigid case were conducted by Wood et al. (2016) and De Nayer et al. (2018). The inflow conditions, the unsteady flow behavior and the characteristic regions of the flow were examined with the help of laser-Doppler anemometry measurements and large-eddy simulations (LES). The problem is now extended to a flexible membranous hemispherical structure for three different Reynolds numbers. The experimental setup and measurements are detailed in Wood et al. (2018). The goal of the present work is to carry out corresponding numerical FSI simulations based on modern eddy-resolving schemes in order to supplement and complete the experimental investigations. Since both methodologies (experiment and simulation) possess specific advantages (and drawbacks), the objective is to exploit especially the higher temporal and spatial resolution of the numerical simulations to enhance the knowledge about the relevant FSI coupling phenomena for flexible membranes in turbulent flows.

The paper is organized as follows: Section 2 introduces the numerical simulation methodology applied. The entire case is detailed in Section 3 followed by the computational setup in Section 4. Section 5 presents the numerical results as a counterpart to the measurements of Wood et al. (2018). The time-averaged data of the first and second-order moments are discussed and especially the unsteady phenomena are investigated. For the sake of brevity, the evaluation of the structure model is shifted to the Appendix.

2. Numerical simulation methodology

The numerical simulation methodology is based on a strong and efficient coupling scheme especially developed for fluid–structure interaction (FSI) problems within turbulent flows. Only a brief summary is presented here since the details are published in Breuer et al. (2012) and corresponding validation studies can be found in De Nayer et al. (2014) and De Nayer and Breuer (2014). Since the method relies on a partitioned procedure, two distinct solvers can be applied: An enhanced version of FASTEST-3D (Durst and Schäfer, 1996) for the computational fluid dynamics (CFD) problem and Carat++ (Bletzinger et al., 2006) for the computational structure dynamics (CSD) problem. In order to couple both codes, the coupling software EMPIRE (Sicklinger et al., 2014) does the mapping between the two diverse surface discretizations at the FSI interface and performs the exchange of the data required by the coupling algorithm.

FASTEST-3D is a fully parallelized finite-volume fluid solver which exploits a predictor–corrector scheme (projection method) of second-order accuracy in space and time. For FSI applications the semi-implicit method was extended to a partitioned coupling scheme which takes the specific needs of LES and FSI into account, i.e., high temporal resolution and strong stability at high fluid-to-structure density ratios (Breuer et al., 2012). The equations are discretized on a curvilinear, block-structured body-fitted grid with a collocated variable arrangement. In the context of FSI applications the temporally varying domain is taken into account by the Arbitrary Lagrangian–Eulerian (ALE) formulation. In order to adapt the mesh to the deformed FSI interface, several methods are available: In case of small deformations a very fast algebraic procedure is performed based on a combination of linear and transfinite interpolations (TFI) (Thompson et al., 1985). If the deformations

[3] http://www.texlon.ch/de/unternehmen/home.htm.
[4] http://www.ketchum.org/shellpix.html.

become significant, a hybrid adaption method especially developed for FSI problems within LES (Sen et al., 2017) is applied. It relies on a combination of an inverse distance weighting interpolation for the block-boundaries of the block-structured grid and a three-dimensional TFI for the inner mesh. Turbulence is taken into account by the LES technique (Breuer, 2002): The large scales in the turbulent flow field are resolved directly, whereas the small scales are modeled by a subgrid scale (SGS) model. As usual in LES, the trace of the SGS tensor τ_{ij} is added to the filtered pressure p: $P = p + \frac{1}{3}\tau_{kk}$. In case of a CFD simulation without any moving wall the term $\frac{1}{3}\tau_{kk}$ is zero on fixed walls and the newly defined pressure P is equal to the real pressure p. In case of FSI, where wall surfaces are moving, the term $\frac{1}{3}\tau_{kk}$ is not zero anymore and a small error is introduced in the computation of the pressure on the moving walls. For the cases presented in this work the relative error $|P - p|/p = \left|\frac{1}{3}\tau_{kk}\right|/p$ always stays below 0.2%. Therefore, the approximation made on the pressure does not really affect the FSI. Moreover, for LES an appropriate representation of the inflow boundary conditions is often necessary (Wood et al., 2016; Breuer, 2018). In FASTEST-3D an inflow generator based on the digital filter concept of Klein et al. (2003) mimics incoming turbulent perturbations. The original concept was extended to permit the superposition of these turbulent perturbations as source terms inside the domain (Schmidt and Breuer, 2017; De Nayer et al., 2018).

Carat++ is a finite-element and isogeometric structure solver developed with emphasis on the prediction of the mechanical behavior of thin-walled structures (i.e., shells and membranes), the structural optimization and form finding procedures for pre-stressed tensile structures (Kiendl et al., 2014; Breitenberger et al., 2015; Philipp et al., 2015). The momentum equation written in a Lagrangian frame of reference is applied to describe the dynamic equilibrium of the structure. The experimental measurements of Wood et al. (2018) show a maximum of the principal strain of about 4.5% for the most critical case at Re = 100,000. Since this value is below the recommended classical limit of 5%, a St. Venant–Kirchhoff material law is assumed. It links the second Piola–Kirchhoff stress tensor with the Green–Lagrange strain tensor. Preliminary considerations to determine the material parameters and post-processing investigations to verify the St. Venant–Kirchhoff model assumption are described in Appendix.

EMPIRE[5] (*Enhanced Multi Physics Interface Research Engine*) is an open-source coupling tool dedicated to co-simulations with n clients ($n \geq 2$). Based on an xml input file the EMPIRE library allows to generate own coupling algorithms such as the classical weak or strong staggered coupling schemes used in FSI applications. More elaborate Jacobian-based coupling procedures can also be defined (Sicklinger et al., 2014). EMPIRE does the mapping between the non-matching CFD and CSD grids and the exchange of data with its clients (Wang et al., 2016). The code relies on the Message Passing Interface (MPI) 2.0 to realize the communication with its clients.

3. Air-inflated flexible hemisphere within a turbulent boundary layer

3.1. Description of the case

As sketched in Fig. 2 a thin-walled membranous structure is mounted on a flat plate and air-inflated in shape of a hemisphere (diameter D). It is exposed to the gravitational acceleration $\mathbf{g} = -9.81\ \mathrm{m/s^2}\ \mathbf{e_z}$ and to a turbulent boundary layer at a Reynolds number of $\mathrm{Re} = D U_\infty \rho_{\mathrm{air}} / \mu_{\mathrm{air}}$ (D = 0.15 m, $\rho_{\mathrm{air}} = 1.225\ \mathrm{kg/m^3}$, $\mu_{\mathrm{air}} = 18.27 \times 10^{-6}\ \mathrm{kg/(m\,s)}$). U_∞ is the undisturbed free-stream velocity in the main flow direction outside the boundary layer at standard atmospheric conditions. The incoming thick boundary layer has a mean velocity distribution according to a 1/7 power law and its thickness δ corresponds to the height of the hemisphere, i.e., $\delta = D/2$. Three different Reynolds numbers (Re = 50,000, Re = 75,000 and Re = 100,000) are investigated, the corresponding velocities U_∞ are 5.14 m/s, 7.64 m/s and 10.24 m/s, respectively. The inflow velocity and turbulence intensity distributions are described in detail by Wood et al. (2018). Since the Mach number is low ($\mathrm{Ma} \leq 0.03$), the air flow can be assumed to be incompressible. Moreover, the fluid is considered to be isothermal.

The properties of the membrane are set to mimic the silicone (Wacker Elastosil 625®) which is used in the experimental studies of Wood et al. (2018). The density is experimentally determined to $\rho_{\mathrm{silicone}} = 1050\ \mathrm{kg/m^3}$. The thickness of the flexible structure is not exactly uniform but varies between 1.2×10^{-4} and 2×10^{-4} m. Numerical predictions based on the average thickness $t_{\mathrm{membrane}} = 1.65 \times 10^{-4}$ m are found to deliver good agreement in comparison with the experiments on pure structural test cases (see Appendix). For the chosen material model only two parameters are necessary: The Young's modulus E_{silicone} and the Poisson's ratio ν_{silicone}. The Young's modulus is experimentally determined to $E_{\mathrm{silicone}} = 7 \times 10^5$ Pa using the tensile test (EN ISO 527–2, see (Wood et al., 2018)). The Poisson's ratio was experimentally evaluated to $\nu_{\mathrm{silicone}} \approx 0.45$ by Wood et al. (2018).

To stabilize the membrane and to match the desired shape of the hemisphere at best, the thin-walled membranous structure has to be air-inflated with an inner pressure difference of $\Delta p_{\mathrm{cal}} = p - p_\infty = 43$ Pa (see the calibration process in Wood et al. (2018) for more details). By increasing the inner pressure difference to a higher value, the structure will not have the hemispherical shape anymore (observable in the steady calibration test case Fig. A.26 of Wood et al. (2018)) and the results obtained could not be compared. In order to enable the development of moderate structural deformations and avoid the formation of deep wrinkles in the membrane for a given flow scenario, Wood et al. (2018) found a compromise and decreased the inner pressure difference to new values Δp_{FSI} depending on the Reynolds number (see Table 1).

[5] http://empire-multiphysics.com.

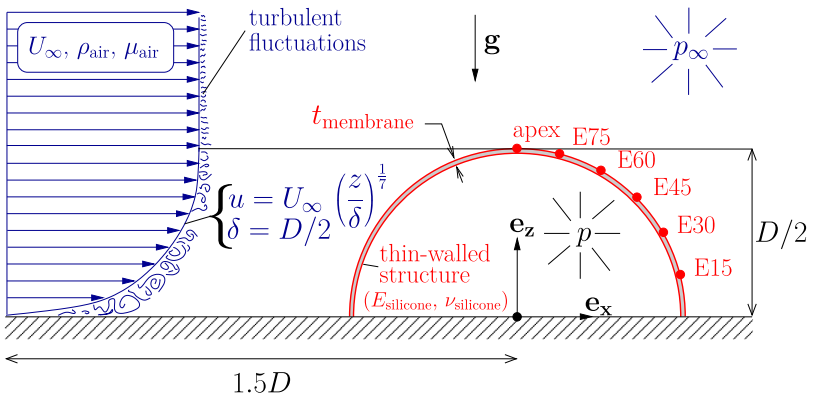

Fig. 2. Pressurized flexible hemisphere within a turbulent boundary layer flow. The red dots are the monitoring points required in Section 5. (For the interpretation of the references to color in this figure legend, the reader is referred to the web version of this article.)

Table 1
Operating conditions for the different Reynolds numbers.

Re	Cy	D [m]	ρ_{air} [kg/m^3]	μ_{air} [kg/(m s)]	U_∞ [m/s]	$\rho_{silicone}$ [kg/m^3]	$t_{membrane}$ [m]	$E_{silicone}$ [Pa]	Δp_{FSI} [Pa]
50,000	4.62×10^{-5}	0.15	1.225	18.27×10^{-6}	5.14	1050	1.65×10^{-4}	7×10^5	19
75,000	1.02×10^{-4}	0.15	1.225	18.27×10^{-6}	7.64	1050	1.65×10^{-4}	7×10^5	35
100,000	1.84×10^{-4}	0.15	1.225	18.27×10^{-6}	10.24	1050	1.65×10^{-4}	7×10^5	43

3.2. Dimensional analysis

A dimensional analysis reduces the problem to the following dimensionless parameters:

- The Reynolds number Re and δ/D for the fluid;
- The length ratio $t_{membrane}/D$ for the geometry;
- $\nu_{silicone}$ for the material;
- The density ratio $\rho_{air}/\rho_{silicone}$, the Cauchy number $Cy = \rho_{air}U_\infty^2/E_{silicone}$ (as defined in de Langre (2002), the ratio $\Delta p_{FSI}/E_{silicone}$, the mean $\overline{\Delta \mathbf{r}}^* = \overline{\Delta \mathbf{r}}/D$ and the standard deviation $\mathbf{S}^* = \mathbf{S}/D$ of the dimensionless displacement vector,[6] the Strouhal numbers $St_i = f_v^i D/U_\infty$ (based on vortex shedding or vortex formation frequencies f_v^i related to the air flow) and the ratios $f_{FSI}^{k,*} = f_{FSI}/f_n^k$ (based on the observed oscillation frequency f_{FSI} and the natural frequencies f_n^k of the structure) for the FSI coupling.

As detailed in Wood et al. (2018), the operating conditions for the fluid (μ_{air}, ρ_{air}, U_∞ and δ) and the diameter of the model D are well defined. The parameters of the structure ($E_{silicone}$, $\nu_{silicone}$ and $\rho_{silicone}$) are carefully evaluated. The thickness of the membrane $t_{membrane}$ cannot be exactly determined. However, an averaged thickness is shown to be a good approximation, which was justified in the complementary experimental measurement campaign. Details on the corresponding investigations and validations are provided in Appendix.

Therefore, the length ratios δ/D and $t_{membrane}/D$, the Poisson's ratio $\nu_{silicone}$, the density ratio $\rho_{air}/\rho_{silicone}$ can be seen as constant and not as parameters of the problem. All the variables composing the Reynolds number Re are well-defined. However, it will be taken as a parameter in order to evaluate its influence on the FSI phenomenon. As the $E_{silicone}$ is constant for all three cases, the Cauchy number Cy is linked to Re and will not be considered as an additional parameter. Moreover, note that for a given Reynolds number, the ratio $\Delta p_{FSI}/E_{silicone}$ is maintained constant (see Table 1).

Thus, the size of the targeted problem is decreased to the following relevant dimensionless numbers: The Reynolds number Re, the mean $\overline{\Delta \mathbf{r}}^*$ and the standard deviation $\mathbf{S}^*$ of the dimensionless displacements, the Strouhal numbers St_i and the frequency ratios $f_{FSI}^{k,*}$.

4. Computational setup

Based on the numerical FSI framework described in Section 2, the computational setup is specified for the current test case.

[6] An alternative definition of the mean $\overline{\Delta \mathbf{r}}^* = \overline{\Delta \mathbf{r}}(2g)/U_\infty^2$ and the standard deviation $\mathbf{S}^* = \mathbf{S}(2g)/U_\infty^2$ of the dimensionless displacement vector is also useful as it introduces a dependency on the fluid velocity (see Section 5.2).

4.1. CFD setup

The CFD solver only solves the domain outside the hemisphere. The constant inner pressure difference Δp_{FSI} is modeled in the CSD solver (see Section 4.2). Therefore, the CFD setup is derived from the investigation of the flow past the rigid hemisphere flow detailed in Wood et al. (2016). The grid is a large hemispherical expansion with its origin at the center of the hemisphere. The outer domain has a radius of 10 D. Analog to Wood et al. (2016) it contains 8 geometrical blocks. 120 grid points are non-equidistantly distributed in the expansion direction and 320 points are placed at the circumference at the bottom of the hemisphere. Compared to the fine reference grid used for the rigid case (30.72×10^6 control volumes (CVs)) this leads to a strong reduction of the grid size (4.3×10^6 CVs). This reduced grid is denoted as *medium* grid in the rest of the study. Similar to Wood et al. (2016) the viscous sublayer is fully resolved and the first cell center is located at a distance of $\Delta z/D \approx 5 \times 10^{-5}$ from the wall. The aspect ratio of the cells on the hemispherical body remains the same as on the fine grid and thus is in the range between 1 and 10. The geometrical stretching ratios are slightly increased compared to those used in Wood et al. (2016) but kept below 1.1. Based on these parameters the dimensionless cell sizes in the wall-normal and tangential directions fit to the recommendation of Piomelli and Chasnov (1996) for wall-resolved LES.

The reduction of the grid size is required in order to carry out the present FSI investigation in a reasonable time. Note that a corresponding study on the grid independence of the flow past the rigid hemisphere of Wood et al. (2016) is provided in De Nayer et al. (2018). Overall the results on the reference and the medium grid show an acceptable agreement concerning the velocity components and the Reynolds stresses.

The boundary conditions for the fluid domain are the same as applied to the rigid case (De Nayer et al., 2018). A no-slip wall is applied at the bottom of the domain and on the hemisphere. In order to mimic the desired incoming boundary layer, a 1/7 power law with $\delta/D = 0.5$ and without any perturbations is set at the inlet patches. To ensure appropriate properties of the incoming turbulence, perturbations are injected as source terms in front of the hemisphere at $x/D = -1.5$. These are generated by the digital filter method mentioned above. For the case Re $= 50{,}000$ the settings of the inflow generator, i.e., the turbulence intensity distributions and the length scales, remain the same as in De Nayer et al. (2018) ($L_{\mathrm{STIG}}/D = 2.06 \times 10^{-2}$ for the wall-normal and spanwise spatial length scales and $T_{\mathrm{STIG}}\, U_\infty/D = 2.79 \times 10^{-2}$ for the integral time scale). The technique applied to inject the fluctuations as source terms is the enhanced formulation introduced in Schmidt and Breuer (2017) and denoted *STIG–R* in De Nayer et al. (2018). Due to the reduced spatial resolution using the medium grid, longer time series could be generated providing better statistics (480,000 time steps instead of 160,000). For the two other cases (Re $= 75{,}000$ and $100{,}000$) the requested time and length scales remain the same as for Re $= 50{,}000$, whereas the turbulence intensity distributions are taken from the measurements presented in Wood et al. (2018).

The outer domain comprises an inlet and an outlet region. To avoid numerical oscillations due to the switch between the inlet and the convective outlet at $x/D = 0$ (where the normal of the face is perpendicular to the main flow direction), the inlet is extended to $x/D \approx 3.3$. Then, for $x/D > 3.3$, a convective boundary condition is applied with a convection velocity determined according to the wall distance applying the 1/7 power law.

In the experimental investigation of Wood et al. (2018) an arithmetic average roughness of $R_a = 16\ \mu$m is measured for the flexible membrane. This leads to a dimensionless value of $R_a^+ = 0.24$, 0.34 and 0.45 for Re $= 50{,}000$, $75{,}000$ and $100{,}000$, respectively. These values are far below 5 and thus in the viscous sublayer ($z^+ \ll 5$). Therefore, no roughness model is required in the simulation.

For preliminary CFD simulations and the subsequent FSI study the subgrid-scale model of Smagorinsky (1963) is applied with a well established standard constant $C_s = 0.1$ and with van Driest damping near the wall. This simple model was shown to be appropriate in Wood et al. (2016). For the spatial discretization, the convective fluxes are approximated by the technique of flux blending (Ferziger and Perić, 2002) to stabilize the simulation (5% first-order accurate upwind scheme combined with 95% second-order accurate central scheme as in Wood et al. (2016). The medium grid and the explicit time integration method used yield small dimensionless time steps of $\Delta t^* = \Delta t\, U_\infty / D = 1.028 \times 10^{-4}$, 4.476×10^{-5} and 3.317×10^{-5} to ensure stable simulations for Re $= 50{,}000$, $75{,}000$ and $100{,}000$ with CFL numbers below unity.

4.2. CSD setup

The thin-walled flexible hemispherical structure is modeled as a membrane due to its very small thickness and thus negligible bending stiffness. Its surface $\Omega \subset \mathbb{R}^3$ is embedded in the 3-D Euclidean space, where $(\mathbf{e_x}, \mathbf{e_y}, \mathbf{e_z})$ stand for the Cartesian basis. The underlying finite-element formulation is a displacement based formulation (Bischoff et al., 2004). The center of the membrane is aligned with the origin of the Cartesian axis, its radius is equal to $R = D/2 = 0.075$ m and its thickness is set to $t_{\mathrm{membrane}} = 1.65 \times 10^{-4}$ m as defined in Section 3.1.

Based on mesh studies related to simple structure cases (see Appendix A.1 and Appendix A.2) the structural domain is discretized by a FEM grid containing 1926 *Constant Strain Triangle* (CST) (Hughes, 2012) elements and 999 nodes (see Fig. A.21(c)). All nodes have 3 degrees of freedom except the ones at $z/D = 0$. These bottom nodes cannot move in any translational direction due to the fact that the membranous structure is attached to the bottom wall. In the experimental setup of Wood et al. (2018) the pressure inside the membrane is maintained nearly constant with the combination of air inlet and outlet drillings, a pressure reducer and a manometer. Thus, the interior of the hemisphere is an open system and the constant inner pressure difference Δp_{FSI} (see Table 1) is modeled in the CSD solver by a follower pressure load acting on each element surface (Schweizerhof and Ramm, 1984). It avoids to solve a CFD problem in the inner domain of the flexible

structure. The gravitational acceleration $\mathbf{g} = -9.81\ \mathrm{m/s^2}\ \mathbf{e_z}$ is also taken into account in the CSD solver as a dead load acting on the volume of each element.

It is typical for membranous structures to be subject to a pre-stress tensor field $\mathbf{n}_0$ in order to render a unique state of static equilibrium, which stabilizes the membrane also in case of additional wind loads. The components of the pre-stress tensor are defined in a local Cartesian coordinate system on the surface of the membrane. In this study, the normal components of the pre-stress tensor are assumed to be constant and equal to n_{membrane} and the shear components are considered negligible. It results in a homogeneous and isotropic pre-stress distribution over the whole structural domain. A separate investigation based on the experimental steady calibration case of Wood et al. (2018) leads to a pre-stress value of $n_{\mathrm{membrane}} = 7794.5$ Pa (see Appendix A.1 for more details).

The time step of the CSD solver is equal to the fluid time step and the classical second-order Newmark scheme is applied. Additionally, the calibrated values of the Rayleigh damping parameters, necessary for modeling the structural damping of the hemisphere are found to be $\alpha = 17.47$ and $\beta = 1.89 \times 10^{-4}$. The damping seems to be high, but for this kind of silicone rubber large damping values have to be expected. They represent the scaling of the mass and the linearized stiffness matrix in the superposition which results in the Rayleigh damping matrix. The procedure for the determination of the Rayleigh damping parameters based on the experimental unsteady structural case of Wood et al. (2018) is presented in Appendix A.2.

4.3. FSI setup

As usual in FSI applications, the CFD and CSD grids are non-matching at the coupling interface. The consistent Mortar mapping method of Wang et al. (2016) is applied. It guarantees a correct exchange of the fluid stresses (tractions) and the structural displacements from one solver to the other.

Both, the loose and the strong FSI coupling schemes are investigated. As expected, their results are very similar. Indeed, since the ratio of the structure density to the fluid density is large ($\rho_{\mathrm{silicone}}/\rho_{\mathrm{air}} \approx 857$), the added-mass effect is not pronounced in the present case (Causin et al., 2005; Farhat et al., 2006). FSI subiterations and an underrelaxation of the displacements are not necessary in contrary to previous FSI-LES investigations, where the ratios between structure and fluid densities were close to unity (Breuer et al., 2012; De Nayer et al., 2014; De Nayer and Breuer, 2014). Since no FSI subiteration are required, significant CPU-time is saved and the loose FSI coupling is preferred.

At the beginning of the coupled simulation the fluid domain is initialized by a pure LES and the structure is stabilized by a higher Young's modulus (7×10^6 Pa) to render the coupled simulation stable. The Young's modulus is slowly decreased during the first 5000 time steps and then stays constant at its correct value of $E_{\mathrm{silicone}} = 7 \times 10^5$ Pa.

The coupled FSI-LES simulation is computed on 40 processors for the CFD part, 1 processor for the CSD part and 1 processor for the coupling part. For Re = 50,000, 75,000 and 100,000, one physical second (i.e., $t^* \approx 34.3$ in dimensionless time) is predicted in about 110, 230 and 610 wall-clock hours, respectively. Each CFD process needs 277 MBytes of RAM storage, the CSD solver 114 MBytes and the coupling program 327 MBytes. That leads to about 11.5 GBytes of RAM storage for one entire simulation.

5. Results and discussion

In order to discuss the turbulent flow around the flexible hemisphere and the associated FSI phenomena, time-averaged numerical results are presented first followed by unsteady ones. The predicted data is averaged over a time interval of $t^* = t\ U_\infty/D = 200$. In the following, the flow field is presented first. Then the behavior of the flexible membrane exposed to the fluid flow is considered. Besides the discussion of time-averaged versus the instantaneous effects, the assessment of the consequences of the structural flexibility is supported by a systematic comparison of the flow fields around the rigid and the deformable hemisphere.

5.1. Time-averaged flow field characteristics

Figs. 3–6 depict the time-averaged streamlines, streamwise normal Reynolds stresses $\overline{u'u'}/U_\infty^2$, wall-normal Reynolds stresses $\overline{w'w'}/U_\infty^2$ and Reynolds shear stresses $\overline{u'w'}/U_\infty^2$ in the symmetry x–z-plane at $y/D = 0$ for Re = 50,000, 75,000 and 100,000 for a rigid and a deformable bluff body. A detailed description of the different characteristic flow regions can be found in De Nayer et al. (2018). Additionally, Table 2 summarizes the time-averaged transition and separation locations in the symmetry plane. In order to determine the position of transition in this plane, a simple method relying on the Reynolds shear stress $\overline{u'w'}/U_\infty^2$ is applied, as it can be considered as a quantity defining the exchange of the momentum into the boundary layer. A threshold for $\overline{u'w'}/U_\infty^2$ is set to -0.001 as used in Schmidt and Breuer (2014). The following discussion focuses on the influence of the Reynolds number on the turbulent flow around the flexible hemisphere.

At a first glance it can be observed that the flow field in the upstream region is similar for all Reynolds numbers and independent of the flexibility of the structure. That has to be expected: Wood et al. (2018) chose nearly matching boundary layers at $x/D = -1.5$ in the experiments and the injected synthetic turbulence data produced by the STIG in the predictions is based on these measurements. Increasing the Reynolds number for the given boundary layer profiles does not change the horseshoe vortex in front of the hemisphere much: The height of the horseshoe vortex slightly decreases and the intensity of its core slightly increases. For the three Reynolds numbers the deformable structure has no visible effect on the upstream

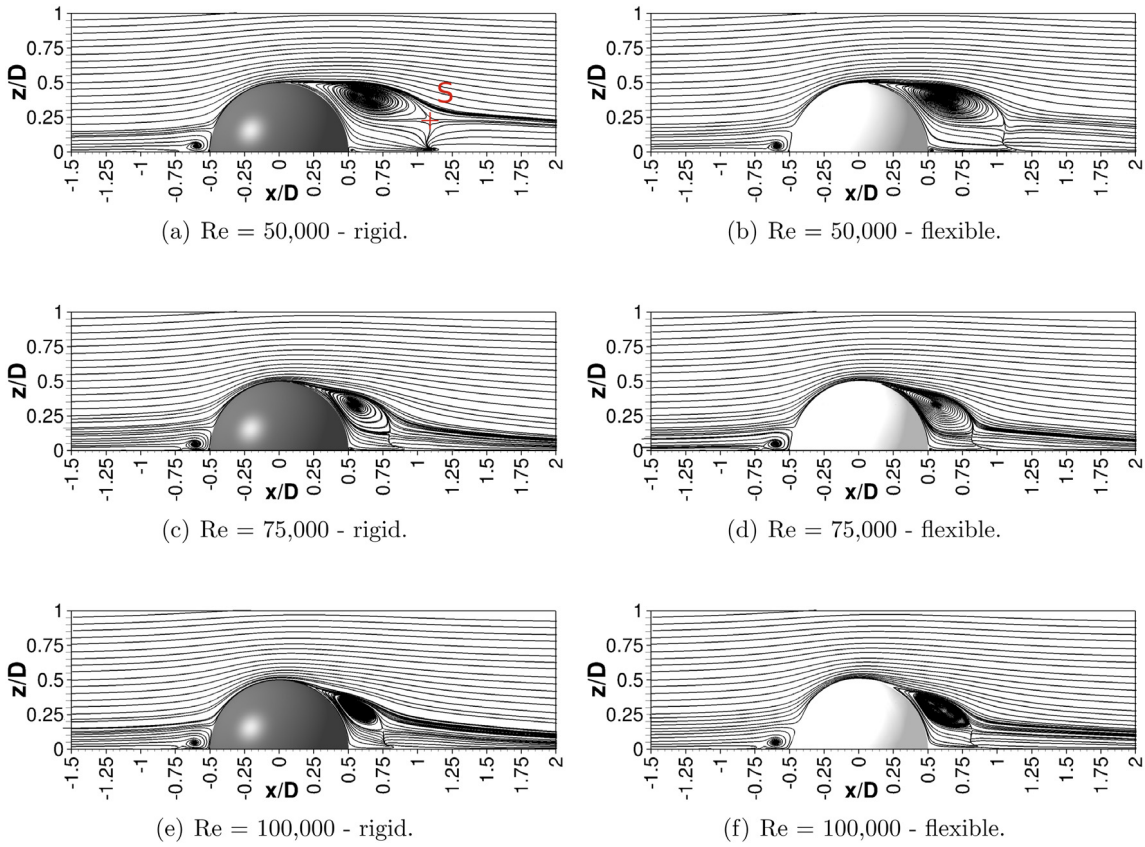

(a) Re = 50,000 - rigid. (b) Re = 50,000 - flexible.

(c) Re = 75,000 - rigid. (d) Re = 75,000 - flexible.

(e) Re = 100,000 - rigid. (f) Re = 100,000 - flexible.

Fig. 3. Comparison of the time-averaged streamlines in the symmetry x–z-plane at $y/D = 0$ predicted by LES for a rigid and a deformable structure.

Table 2
Time-averaged transition and separation locations in the midplane.

Flow characteristics		Transition		Separation	
		x_{tra}/D	z_{tra}/D	x_{sep}/D	z_{sep}/D
Rigid	50,000	3.11×10^{-2}	5.05×10^{-1}	4.15×10^{-3}	5.00×10^{-1}
	75,000	-1.01×10^{-3}	5.09×10^{-1}	4.88×10^{-2}	4.98×10^{-1}
	100,000	-7.25×10^{-3}	5.07×10^{-1}	7.05×10^{-2}	4.95×10^{-1}
Flexible	50,000	2.65×10^{-2}	5.04×10^{-1}	3.59×10^{-3}	4.99×10^{-1}
	75,000	-4.59×10^{-3}	5.12×10^{-1}	3.88×10^{-2}	5.02×10^{-1}
	100,000	-1.26×10^{-2}	5.19×10^{-1}	4.96×10^{-2}	5.08×10^{-1}

region even if the deformation is quite large in this region for Re = 100,000. The height of the boundary layer and of the horseshoe vortex remain nearly the same compared to the results of the rigid case.

Contrary to the upstream region significant differences are visible in the downstream region:

First, the results for the *rigid hemisphere* are discussed: An increasing Reynolds number leads to a strong reduction of the recirculation area. The increase of the Reynolds number affects the mean location of transition which moves upstream with rising Re leading to a stronger mixing and higher turbulence intensities in the region downstream. Consequently, the separation line on the hemisphere is shifted downstream and the flow detaches later from the bluff body and closer to the bottom wall. The streamlines in the shear layer are stronger inclined towards the bottom and the flow reattaches closer to the bluff body. The separated shear layer visible by the distributions of the Reynolds stresses is also impacted. With increasing Reynolds number the region of high turbulence intensity becomes shorter, but develops closer to the hemisphere. The extrema of the Reynolds stresses in this area increase with the Reynolds number. These changes in the recirculation area have consequences in the flow topology downstream: At Re = 50,000 a horizontal dividing streamline is observable in Fig. 3(a) with a remarkable saddle point (denoted S). Starting from Re = 75,000 this dividing streamline is no more horizontal and the saddle point moves towards the ground and closer to the bluff body.

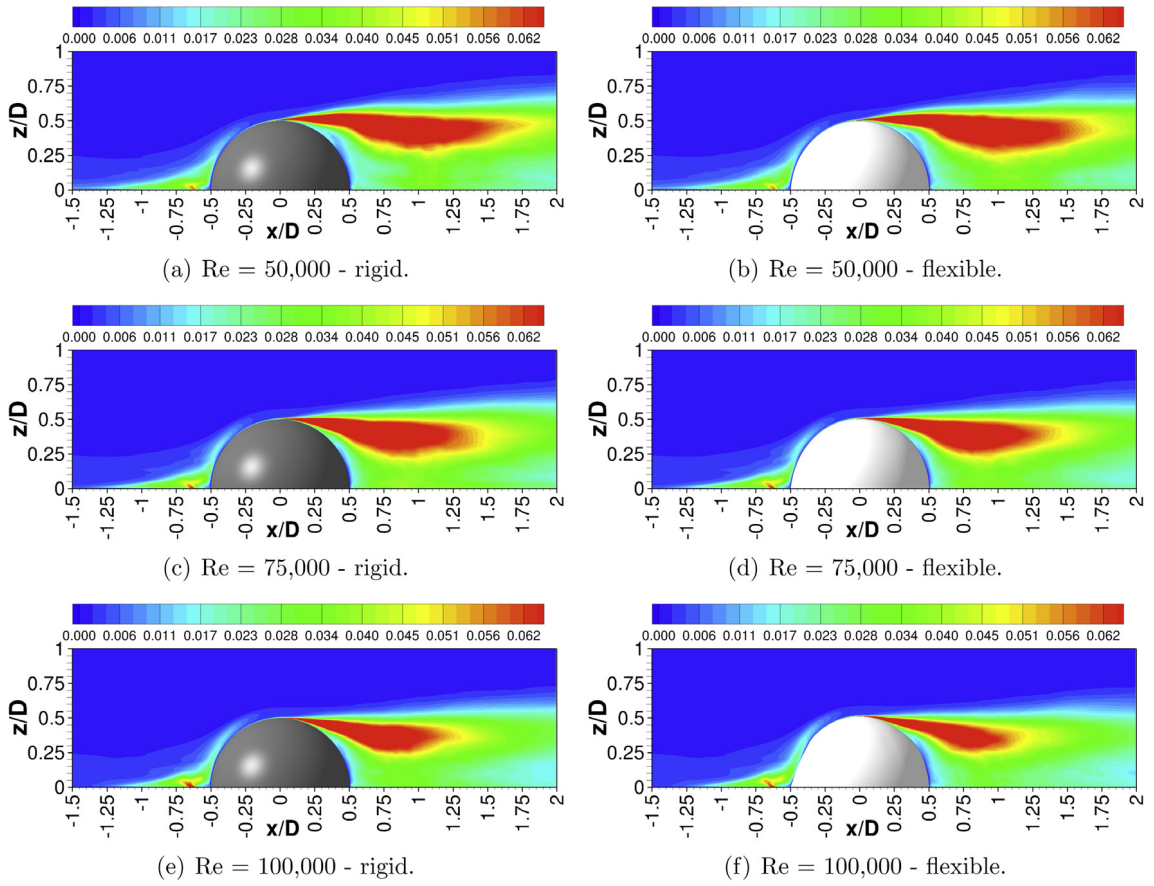

Fig. 4. Comparison of the time-averaged streamwise normal Reynolds stresses $\overline{u'u'}/U_\infty^2$ in the symmetry x–z-plane at $y/D = 0$ predicted by LES for a rigid and a deformable structure.

Second, the results for the *flexible hemisphere* are discussed and compared to the rigid reference respectively: At Re $=$ 50,000 the transition and separation positions, the time-averaged streamlines and Reynolds stresses are nearly identical for the flexible and the rigid case. The small deformations of the hemispherical membrane explain this observation. Increasing the Reynolds number the recirculation area and the region of high turbulence intensity again become shorter similar to the rigid case. However, some differences between the rigid and the flexible case appear: For the latter the position of transition and separation moves upstream and slightly vertically along the membranous structure. It implies that the saddle point in the wake moves less towards the ground than for the rigid case. The dividing streamline is located at a larger distance from the bottom wall and is less inclined than for the rigid case (particularly visible at Re $=$ 100,000). At Re $\geq$ 75,000 the zone of high turbulence intensity in the recirculation area is slightly attenuated near the flexible structure and in the wake compared to the rigid configuration.

For both rigid and flexible configurations the separation seems to be laminar at Re $=$ 50,000. Please note, however, that both locations are really close to each other for this case and that the method to determine the position of transition is only based on a rather simple threshold criterion. Taking these restrictions into account, the separation is turbulent at Re $=$ 75,000 and 100,000.

All these observations are in agreement with the conclusions of Wood et al. (2018). However, a direct comparison of the time-averaged streamlines shows some deviations in the downstream region for Re $\geq$ 75,000. For the rigid case the topology of the flow behind the bluff body differs: The saddle point has already disappeared at Re $=$ 75,000 in the experimental data. Another difference of the rigid case is that the length of the recirculation area predicted by LES is found to be shorter than in the measurements. For the flexible case the topology of the flow behind the bluff body fits the measurements. However, the dividing streamline is found at a position closer to the ground in the simulations at Re $\geq$ 75,000, whereas it remains at the same height throughout the wake for the experiment independent of the Reynolds number. A possible reason for these minor deviations in the recirculation area and in the wake at Re $\geq$ 75,000 is the combination of the *medium* grid with the fixed-coefficient SGS model of Smagorinsky. The *medium* grid satisfies the classical wall resolution requirements for the three Reynolds numbers investigated, therefore the boundary layer is correctly resolved in the three

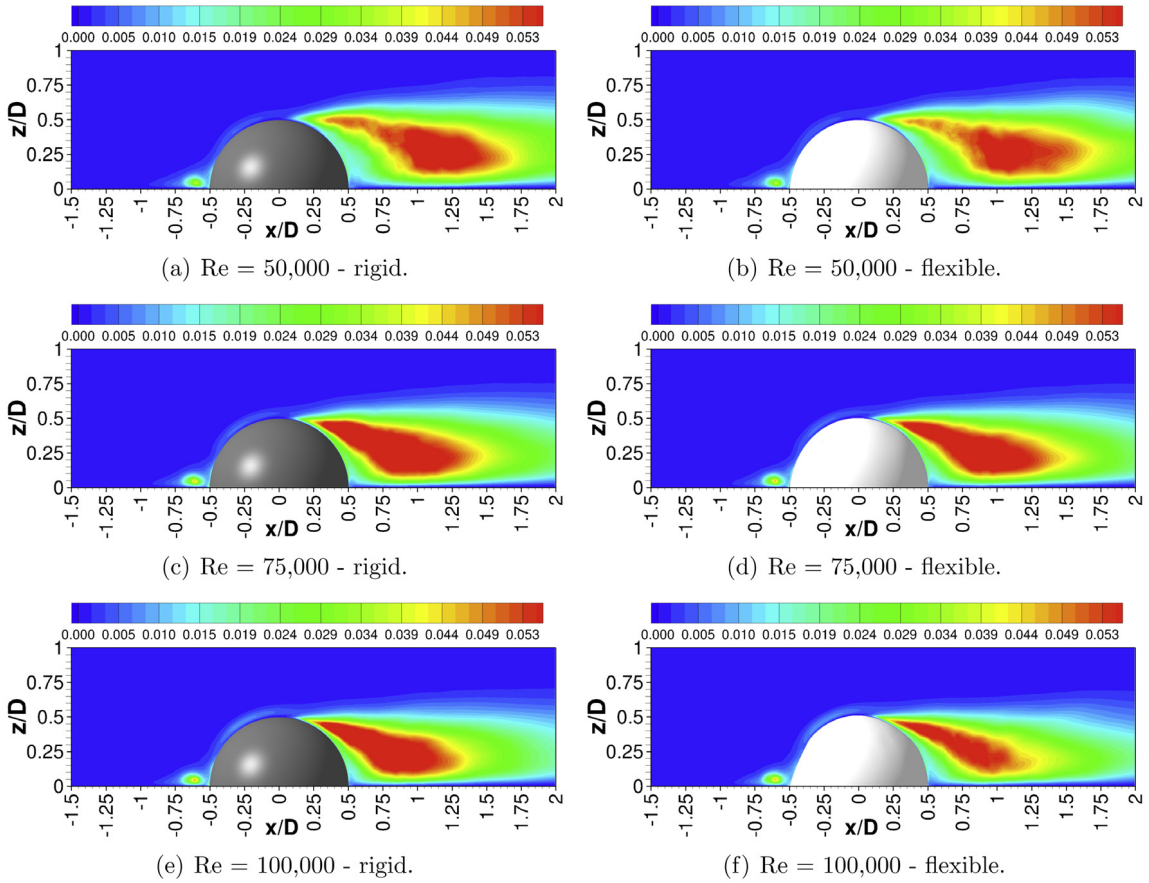

Fig. 5. Comparison of the time-averaged wall-normal Reynolds stresses $\overline{w'w'}/U_\infty^2$ in the symmetry x–z-plane at $y/D = 0$ predicted by LES for a rigid and a deformable structure.

cases. By moving away from the walls the *medium* grid becomes coarser and the SGS model plays a major role in these regions. In preliminary studies (De Nayer et al., 2018) this SGS model was proved to be sufficient on the *medium* grid for Re = 50,000. However, the influence of the SGS model becomes more important, when the Reynolds number increases. It has to model a larger part of the spectrum of turbulent scales. The combination of a relatively coarse resolution in a region of the domain (for instance the wake) with an increase of the Re number leads to larger errors. Moreover, the fixed-coefficient SGS model of Smagorinsky is not ideal for transition prediction, which can impact the shape of the recirculation area and the wake.

To better comprehend the three-dimensionality of the time-averaged flow and to provide supplementary information in comparison to the experiments, the time-averaged wall streamlines are depicted in Fig. 7. Fig. 8 is a close-up top and side view of the time-averaged streamlines on the surface of the flexible hemisphere in combination with the time-averaged fluid pressure coefficient $c_p = (p - p_\infty)/(\rho_{\text{air}} U_\infty^2/2)$. Only the flexible case is presented, since no significant difference between the rigid and the flexible case is visible for a given Re. A plot of the time-averaged wall streamlines around the rigid body at Re = 50,000 and a detailed description of its characteristics can be found in Wood et al. (2016). Since the incoming flow has the same velocity profiles, same Reynolds stress distributions and same length scales for all three Re investigated, the upstream and side patterns of the time-averaged wall streamlines remain identical. For Re $\geq$ 75,000 the wake flow is influenced by the flexible membrane as seen before in the symmetry plane. However, the flexibility of the structure seems to have a minimal impact on the flow in the x–y-plane near the bottom wall: For a given Re the detachment line on the structure moves upwards, but the distribution of the time-averaged wall streamlines does not change much. With or without the flexible hemisphere the recirculation area shortens with increasing Re. Only one alteration of the flow topology near the wall is observed by increasing Re: At Re = 50,000 a small counter-rotating vortical structure visible in Fig. 8(a) is present on the hemisphere after the separation line (also noticed in Wood et al. (2016)). It disappears at Re $\geq$ 75,000 for the rigid and flexible hemisphere.

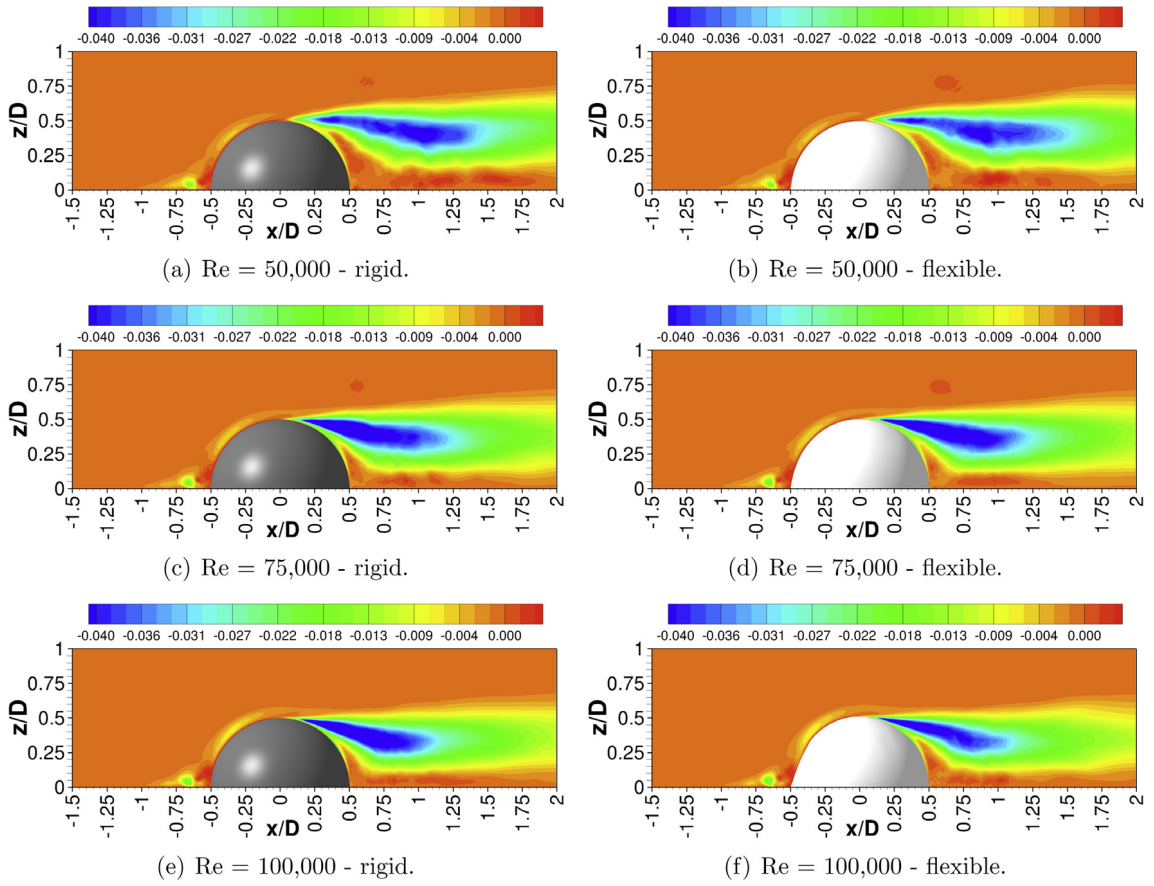

Fig. 6. Comparison of the time-averaged shear Reynolds stresses $\overline{u'w'}/U_\infty^2$ in the symmetry x–z-plane at $y/D = 0$ predicted by LES for a rigid and a deformable structure.

5.2. Time-averaged deformation characteristics

To characterize the whole FSI problem the time-averaged deformation of the flexible membrane is also of interest. Fig. 9 gathers this quantity in the symmetry plane for the three Reynolds numbers studied. Since the deformations are rather small even at Re = 100,000, a magnification factor of $a = 3$ is applied to the average displacements $\overline{\Delta x}/D$ and $\overline{\Delta z}/D$ and added to the reference configuration.

At Re = 50,000 the shape of the deformable structure is nearly identical to the rigid one. The pressure and the shear stress distribution generated by the flow is not strong enough compared to the imposed inner pressure and the gravity to generate perceptible deflections. For all Reynolds numbers deformations are not visible near the bottom wall due to the fixed boundaries. However, at the apex the flexible membrane vertically deforms with increasing Reynolds number. This is due to two factors:

- The flow deflected by the bluff body and accelerated in the region above the apex of the hemisphere induces a low pressure region on the top (see Fig. 8) leading to a vertical lift force.
- The approaching flow impacts on the structure at the stagnation area deforming the flexible structure in shape of an indentation. As the inflated structure is closed and the inner pressure is assumed to be constant, the membrane has to react to this indentation and thus expands on the sides and on the top.

The time-averaged deformations for the three Reynolds numbers are in good agreement with the measurements of Wood et al. (2018), in particular near the apex.

The fluctuations of the displacements $\Delta x/D$ and $\Delta z/D$ are compared for the three Reynolds numbers based on the dimensionless standard deviations $S_x^* = S_x/D$ and $S_z^* = S_z/D$ in Fig. 10. The shape of S_x^* is comparable for the three Re: The standard deviations are low and quasi constant in the upper part of the hemisphere. Towards the border of the membrane, it increases reaching a maximum and abruptly decreases to zero at the clamping of the bottom wall. The global distribution of the numerically predicted quantity S_x^* is in agreement with the experimental data. However, the maxima are not exactly

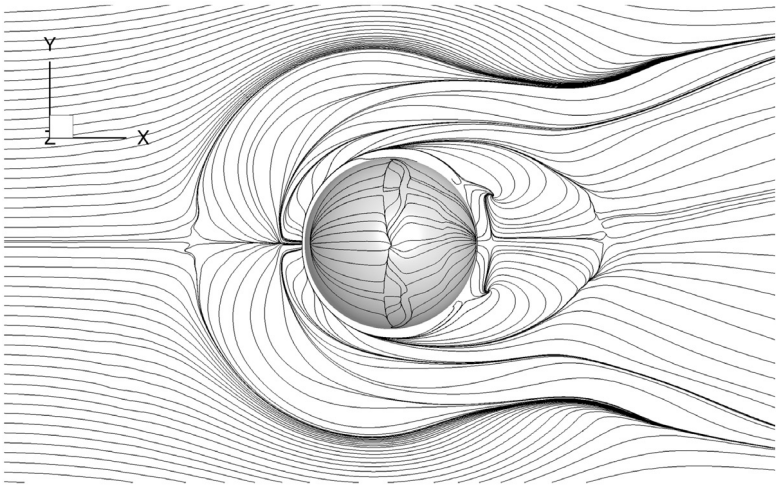

(a) Re = 50,000.

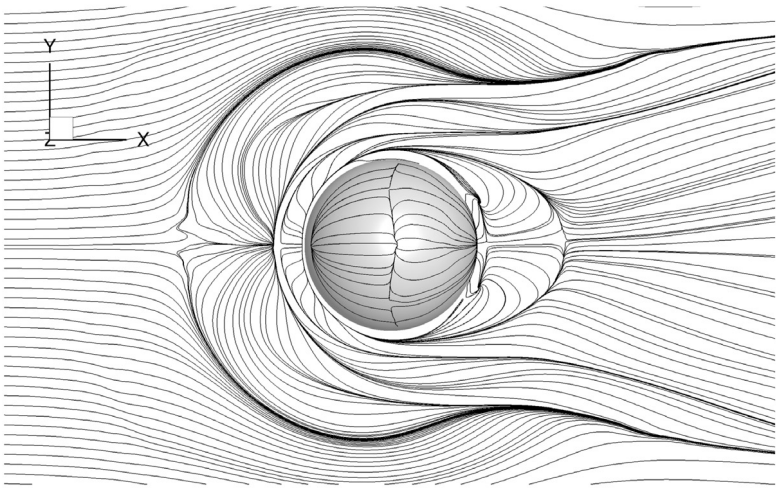

(b) Re = 75,000.

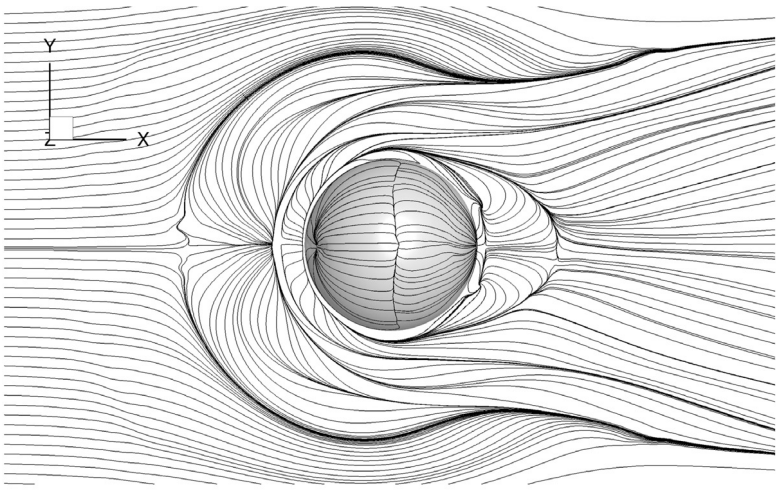

(c) Re = 100,000.

Fig. 7. Time-averaged streamlines near the bottom wall and on the surface of the flexible hemisphere.

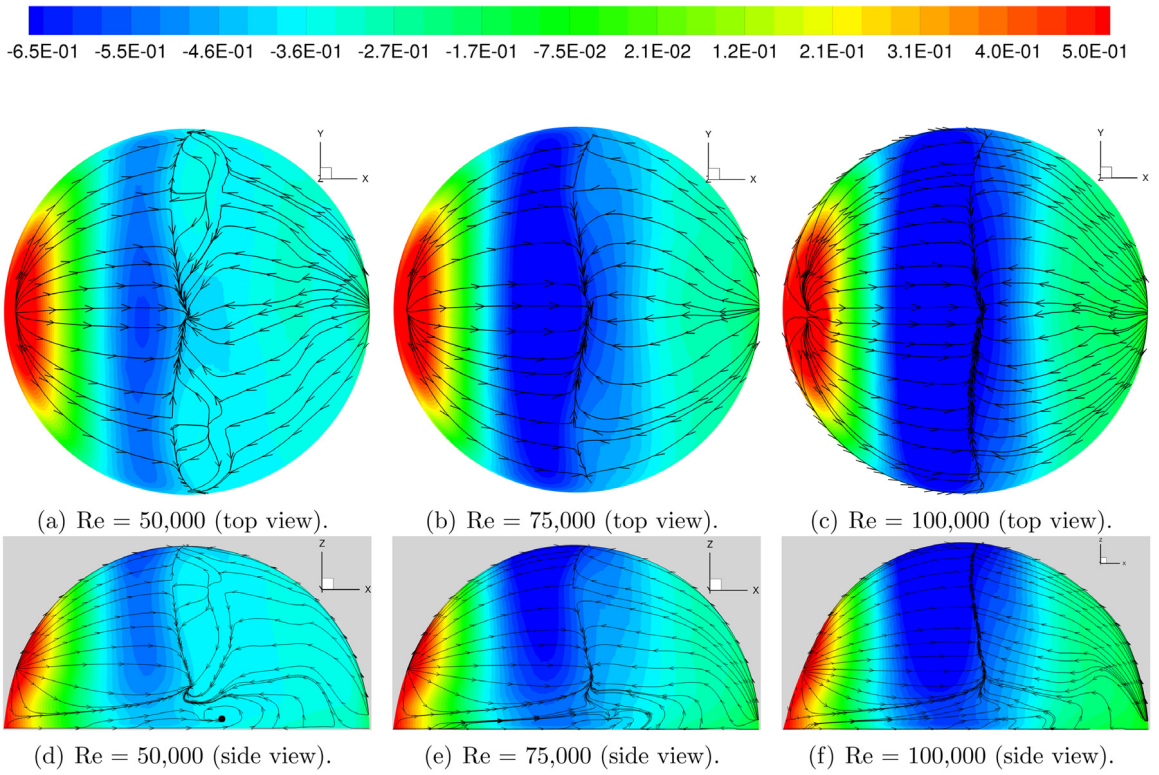

Fig. 8. Time-averaged fluid pressure coefficient $c_p = (p - p_\infty)/(\rho_{\text{air}} U_\infty^2/2)$ with wall streamlines on the flexible FSI interface.

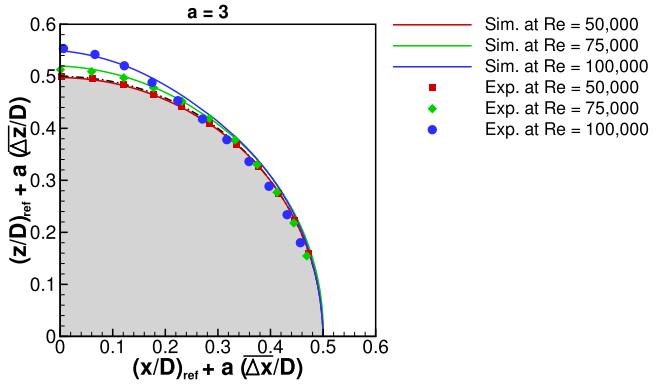

Fig. 9. Comparison of the time-averaged deformation of the flexible hemisphere in the symmetry plane in the wake region for the three Reynolds numbers investigated. A magnification factor of $a = 3$ is applied to the average displacements $\overline{\Delta x}/D$ and $\overline{\Delta z}/D$ and added to the reference configuration to highlight the differences in shape.

at the same location. In the simulation the maxima are found further downstream compared to the measurements. The amplitude of the predicted S_x^* are also larger than in the experiments (about two times), but of the same order of magnitude. S_z^* also shows the same order of magnitude for the FSI predictions and the measurements. However, the predicted shape deviates from the experimental one: Similar to S_x^*, S_z^* is approximately constant near the apex. Then, contrary to the measurements, the maxima are reached at a lower part of the body, before the values drop to zero at the boundary. This behavior can be linked to the dynamic behavior of the applied membrane model presented in Appendix A.2. The present FEM structure model shows a dominant eigenmode (EM) around 62 Hz instead of 78 Hz in the experiments. The representation of the eigenmodes based on a linear modal analysis in Appendix A.3 corresponding to 62 Hz, i.e., EM 11 to EM 14 (see Fig. A.28(g) and (h)) shows four expansions and four contractions at an angle of about 45° similar to the maxima of the S_z^* of

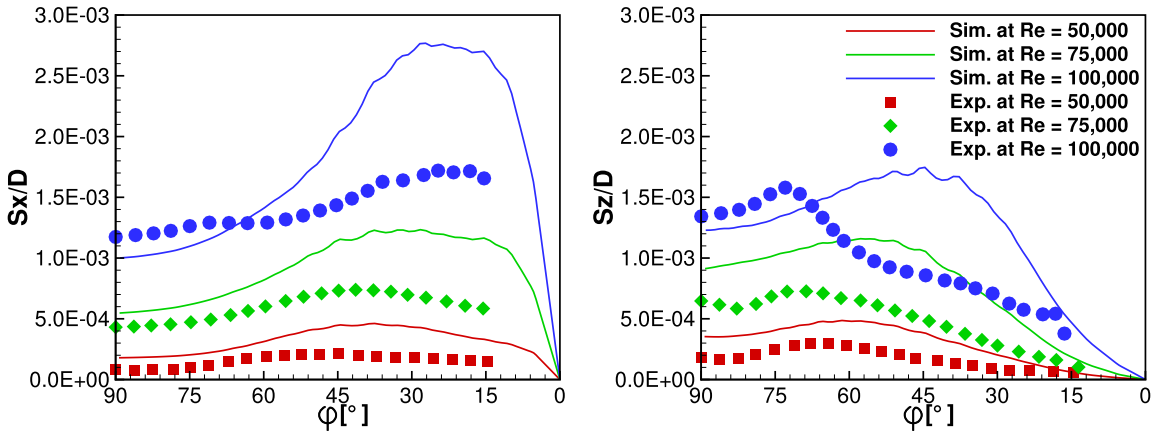

Fig. 10. Standard deviation S_x^* and S_z^* of the corresponding displacements.

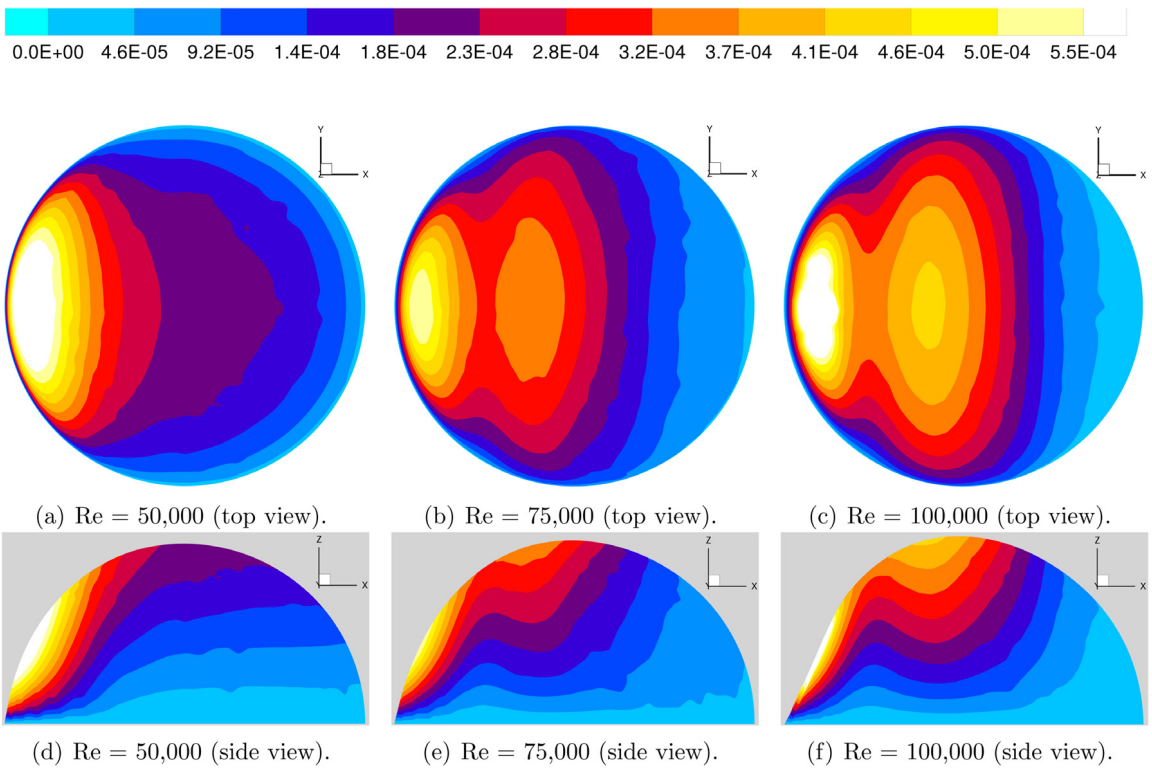

Fig. 11. Time-averaged three-dimensional total deformations $|\Delta\mathbf{r}|$ of the flexible hemisphere normalized by $U_\infty^2/(2g)$.

the FSI simulations (see Fig. 10). The eigenmodes at the frequency 78 Hz, i.e., EM 31 to EM 34 (see Fig. A.28(j) and (k)) reveal strong expansions at a higher angle around 70° similar to the maxima of the S_z^* in the experiments of Wood et al. (2018).

In order to better understand the three-dimensionality of the time-averaged deformation and to provide supplementary informations in comparison with the experiments, the time-averaged three-dimensional total deformation $|\Delta\mathbf{r}| = \sqrt{\Delta x^2 + \Delta y^2 + \Delta z^2}$ of the flexible hemisphere is depicted in Fig. 11. To compare the time-averaged total deformation of the three Reynolds numbers based on the same contour levels and without a magnification factor, a normalization by $U_\infty^2/(2g)$ is applied. Contrarily, a normalization of the total displacements based on the constant geometric quantity D leads to a wide data range, which is not comparable using the same contour levels. Thus, a normalization according to $(\rho_{\text{air}}\, U_\infty^2/2)\ /\ (\rho_{\text{air}} g) = U_\infty^2/(2g)$ is chosen, since the maximum of the dynamic pressure is linked to the maximum of the total deformation at the stagnation area in front of the body.

For Re = 50,000 the largest total deformations take place at the front of the bluff body, where the stagnation area is found. The flow pressure visible in Fig. 8(a) leads to an inward indentation of the flexible interface. A low rotationally symmetric total deformation is observed on the back of the hemisphere and the iso-lines of the deformation are quasi parallel to the bottom wall. Starting with Re = 75,000 a drastic change in the total deformation pattern occurs, where two regions with local maxima appear: The first corresponds to the stagnation area of the flow similar to the observations at Re = 50,000. The second is located at the upper side of the flexible hemisphere, slightly upstream of the apex. Contrary to the first area the second corresponds to an expansion of the body outwards linked to the large area of strong negative pressure coefficient visible in Fig. 8(b) and (c). Moreover, the total deformations on the back of the body are no longer rotationally symmetric. The form of the flexible structure is more altered on the top and on the sides than on the back due to the larger zone of negative pressure coefficient. At Re = 100,000 the total deformation pattern remains similar, but the local maxima of the total deformations and the expansion at the sides and at the back of the body increase.

The fluctuations of the displacements are also investigated and depicted in the same manner as the deformations. The standard deviations for the streamwise and vertical displacements are plotted in Fig. 12. As for the time-averaged total deformations a normalization based on $U_\infty^2/(2g)$ is necessary to enable a comparison using the same contour levels. This time the patterns of the dimensionless standard deviations stay similar for the three Reynolds numbers. The stagnation region in the front and the recirculation region at the back of the hemisphere exhibit the highest streamwise standard deviation. By increasing Re the local maxima of S_x^* increase. For the vertical standard deviation only one major region of high values is found on the back of the hemisphere. By increasing Re the maximum of S_z^* moves downwards towards the bottom wall. Note that for Re = 100,000 noteworthy fluctuations of the displacements in streamwise and vertical directions are also present in the stagnation area.

The total velocity of the FSI interface derived from the displacements is low. Furthermore, the values of the Reynolds stresses found on the surface are also small. Therefore, it seems that the fluctuations of the membrane have a minor impact on the changes observed in Section 5.1 between the flow fields of the rigid and the flexible hemisphere. Thus, these variations are more dominated by the time-averaged deformation of the structure.

5.3. Instantaneous fluid–structure interaction phenomena

Wood et al. (2018) showed that the fluid–structure interaction of the present flexible hemisphere is fully three-dimensional and highly time-dependent. Thus, a discussion relying solely on the time-averaged data is not enough to comprehend the current coupled problem. Moreover, the observed main FSI phenomena are concentrated mainly on the back of the hemisphere. The formation and shedding of vortices at defined Strouhal numbers behind the bluff body leads to large deformations of the membrane. The flexible structure is excited by the turbulent flow and some of the dominant FSI frequencies are related to natural frequencies of the hemisphere. However, due to the non-synchronized flow and structure measurements carried out by Wood et al. (2018), it was impossible to directly link the structure deformation to a particular flow phenomenon. The present analysis based on the coupled simulations does not have this drawback building a bridge between experiments and numerics. This section summarizes the FSI phenomena related to the predicted fluid motion and those related to the predicted structure deformations. The numerical results are compared with the experimental data. To complement the measurements and to better understand these instantaneous phenomena, three-dimensional visualizations of the dominant flow structures and membrane deformations are considered.

Similar to Wood et al. (2018) the fluid–structure interactions are tracked with the help of FFT of the deformations of the flexible membrane. Fig. 13 presents the power spectral density (PSD) of each deformation component for each Reynolds number at the same six monitoring points as in the experiment (see red dots in Fig. 2). The PSD based on the simulations are in good agreement with those of Wood et al. (2018): The shape of the curves and the PSD amplitudes are similar. The order of the curves of the predicted data remains the same as for the experiment. These are first indicators that the simulations are reliable.

In each PSD graph of Fig. 13, remarkable FSI frequencies can be noted. These can be classified into two categories: those related to the fluid flow and those related to the structure deflections.

5.3.1. FSI frequencies related to the fluid flow

The preliminary investigations of the turbulent flow field around the rigid hemisphere at Re = 50,000 conducted by Wood et al. (2016) detected two different vortex shedding types at the sides of the body:

- A symmetric vortex shedding in the Strouhal number range $0.21 < \mathrm{St} < 0.33$.
- An antisymmetric von Kármán vortex shedding at St = 0.16;

Fig. 14(a) and (b) illustrate both shedding types based on the velocity magnitude near the bottom wall. In order to better outline both shedding types more comprehensively they are schematically depicted in Fig. 14(c) and (d). These two vortex shedding processes are not simultaneously present in the flow. They randomly alternate in time at the sides of the bluff body as highlighted in Fig. 14(e).

In order to better comprehend the symmetric vortex shedding, the instantaneous three-dimensional vortical structures behind the hemisphere are visualized based on the iso-surface of the fluid pressure coefficient $c_p = (p - p_\infty)/(\rho_{\mathrm{air}} U_\infty^2/2) =$

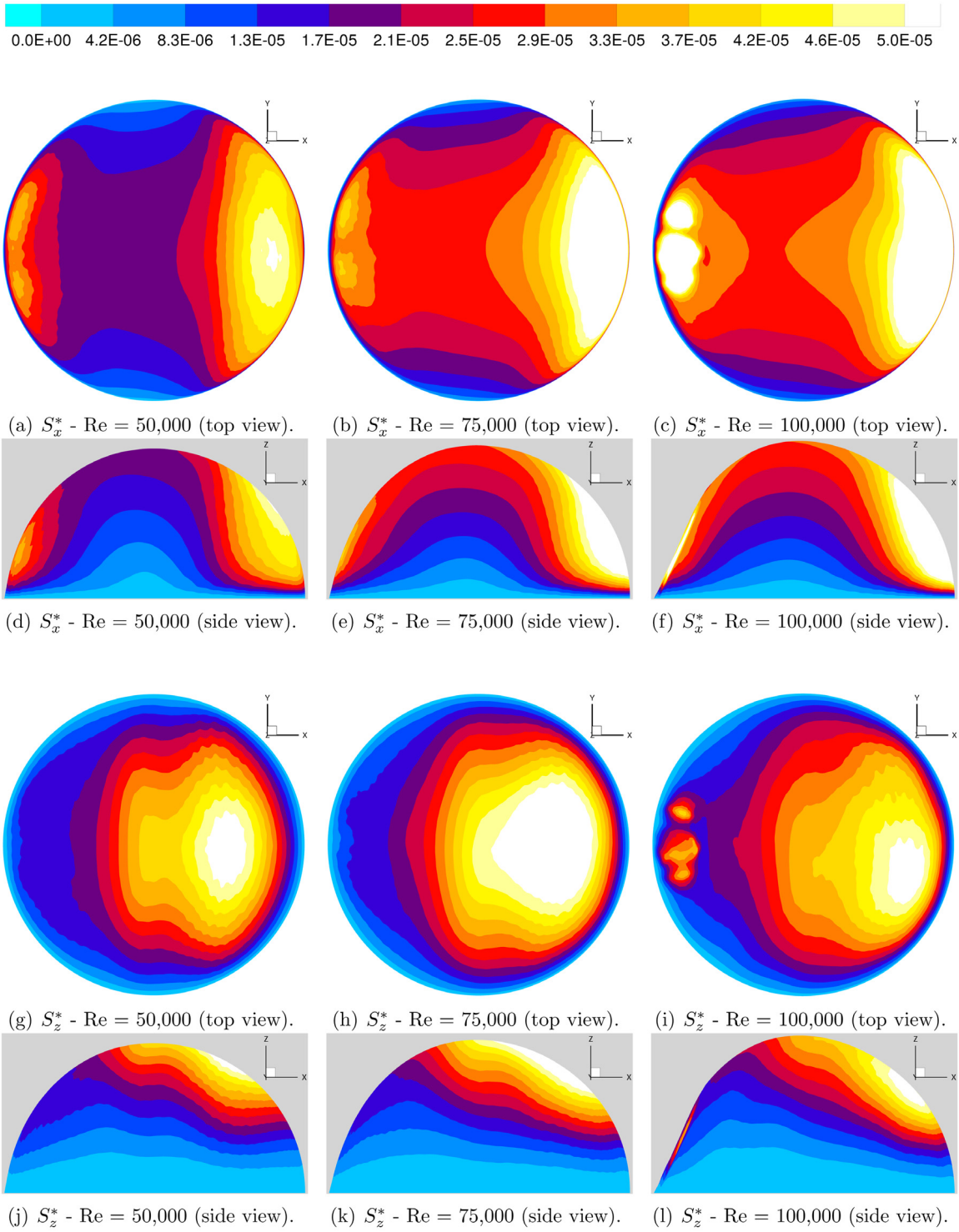

Fig. 12. Time-averaged three-dimensional standard deviations of the total deformations of the flexible hemisphere normalized by $U_\infty^2/(2g)$.

−0.48 in Fig. 15. This shedding phenomenon implies vortical structures of arc-type form, which detach in a "double-sided" symmetric manner.

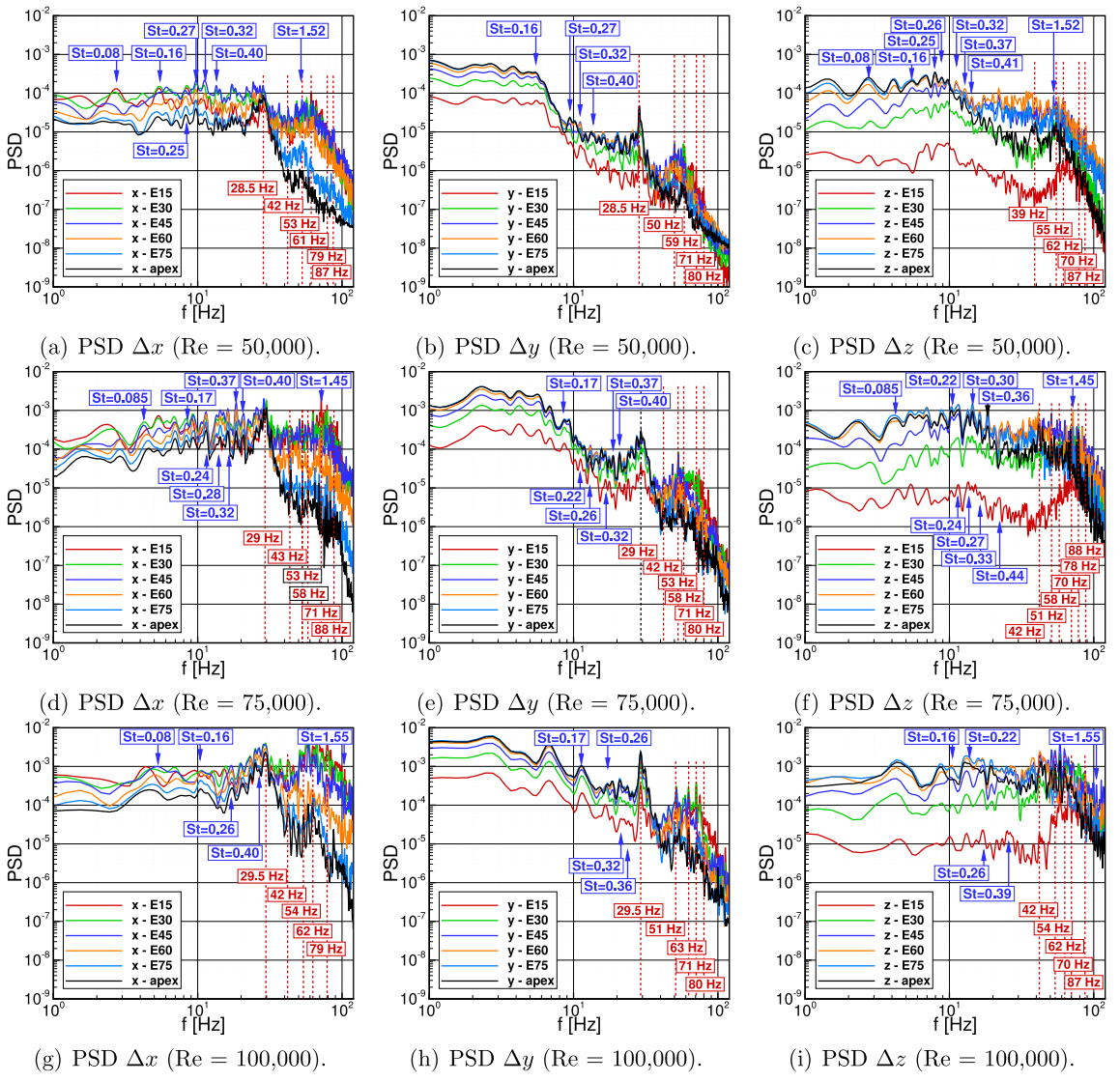

Fig. 13. Power spectral density of the deformations taken at the east-side monitoring points and at the apex of the flexible hemisphere. The east-side monitoring points are the red points in Fig. 2.

The same method is applied for the von Kármán vortex shedding. Fig. 16 depicts the iso-surface of the fluid pressure coefficient $c_p = -0.48$ and highlights the instantaneous three-dimensional large vortical structure which detach in an alternating manner from one side of the body. In this process the vortical structure is quasi vertical and its height is correlated with the height of the recirculation area. With increasing Re, the recirculation area becomes shorter and smaller. Consequently, that results in a smaller von Kármán vortex as visible in Fig. 16(a)–(c).

Both shedding types are now visualized in combinations with the vertical structure deformations of the membranous structure at the rear side. Fig. 17 presents the instantaneous vertical deformations normalized by $U_\infty^2/(2g)$ resulting from the shedding of symmetric arc-type vortices (highlighted by the fluid pressure coefficient c_p near the bottom wall and marked by square symbols) for the three Reynolds numbers investigated. Similarly, Fig. 18 summarizes the instantaneous vertical deformations normalized by $U_\infty^2/(2g)$ corresponding to the von Kármán shedding. For Re = 50,000 the resulting deformations in case of both sheddings are too small to be clearly visualized (see Fig. 17(a)–(c) and Fig. 18(a)–(c). However, at Re = 75,000 and Re = 100,000, it can be clearly seen that a symmetric shedding leads to a quasi symmetric vertical deformation (see Fig. 17(d), (e), (g), and (h). Similarly, a von Kármán shedding results in an asymmetric vertical deformation of the membrane (see Fig. 18, (d), (e), (g), (h) and (i).

The shedding of a symmetric arc-type vortex generates a symmetric deformation on the rear side of the flexible hemisphere as seen in Fig. 19: The core of the vortex is marked by a square symbol. This deformation is characterized

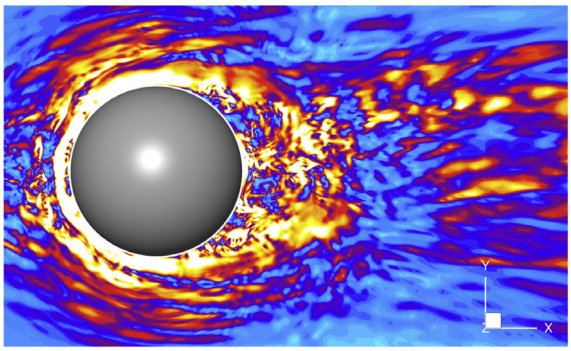

(a) Symmetric shedding type (velocity magnitude near the bottom wall).

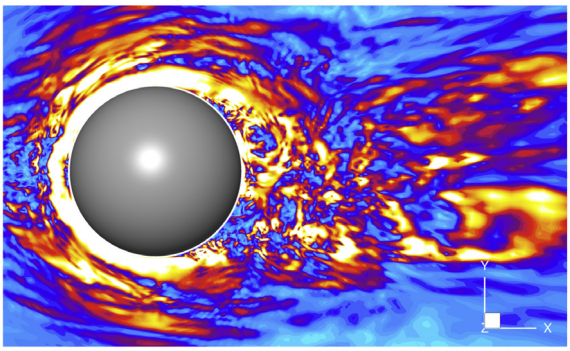

(b) Von Kármán shedding type (velocity magnitude near the bottom wall).

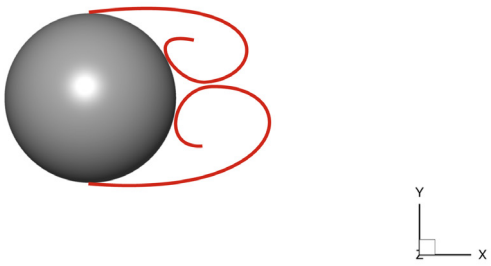

(c) Schematic of the symmetric shedding type.

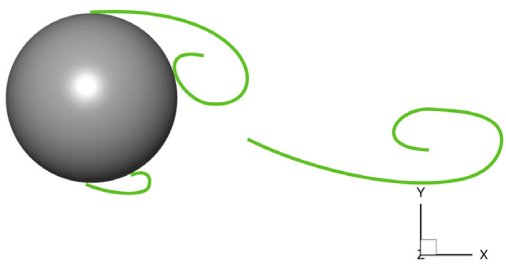

(d) Schematic of the von Kármán shedding type.

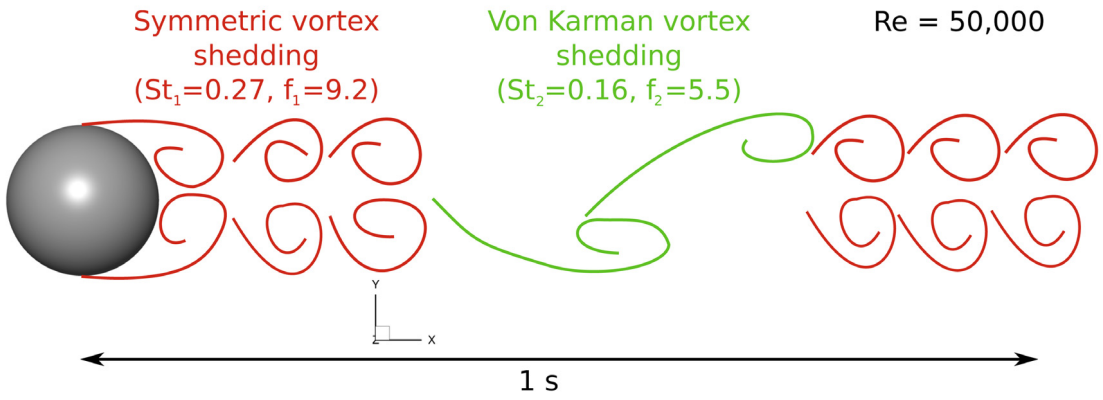

(e) Example of the alternation in time of both shedding types.

Fig. 14. Visualization of the two large-scale vortex shedding types present in the wake behind the rigid hemisphere near the wall for Re = 50,000 (Wood et al., 2016).

by a global expansion of the rear side of the hemisphere in streamwise direction. The flexible structure is sucked up by the shedding of the large vortex. When the symmetric arc-type vortex moves downstream, the induced expansion shifts downwards and gradually looses its magnitude.

The frequencies resulting from both shedding types are clearly visible for the three Reynolds numbers in each PSD of Fig. 13. The von Kármán vortex shedding can be noticed in all displacement components at St $\approx$ 0.16 for Re = 50,000, 75,000 and 100,000. These values match very well the experimental data by Wood et al. (2018). The corresponding frequency is related to the deformations resulting from the drag force variations. Since the von Kármán vortex shedding is asymmetric, a second frequency, half of the above-mentioned, related to the deformations resulting from the lateral force variations, is also present. Therefore, Strouhal numbers at St $\approx$ 0.08 are also marked in Fig. 13. This second value is not mentioned in Wood

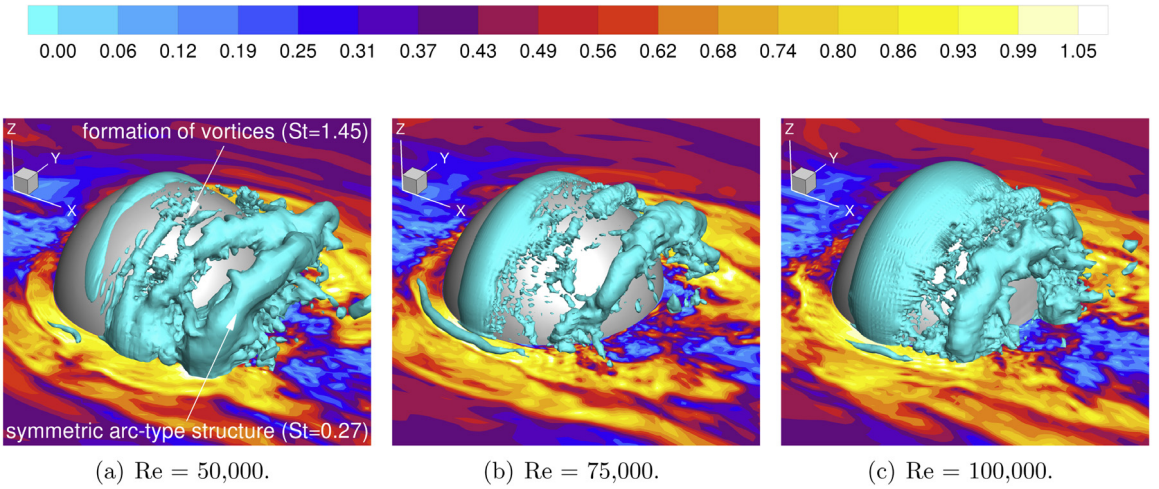

(a) Re = 50,000. (b) Re = 75,000. (c) Re = 100,000.

Fig. 15. Visualization of the instantaneous three-dimensional vortical structures at the back of the flexible hemisphere in case of the symmetric shedding type (velocity magnitude near the bottom wall normalized by U_∞ and iso-surface of the fluid pressure coefficient $c_p = (p - p_\infty)/(\rho_{\text{air}}\, U_\infty^2/2) = -0.48$).

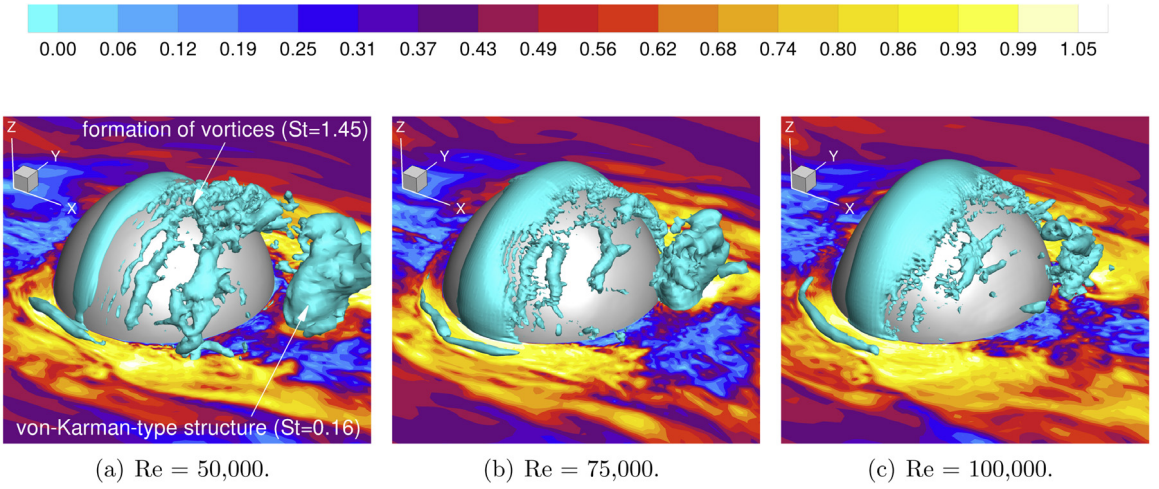

(a) Re = 50,000. (b) Re = 75,000. (c) Re = 100,000.

Fig. 16. Visualization of the instantaneous three-dimensional vortical structures at the back of the flexible hemisphere in case of the von Kármán shedding type (velocity magnitude near the bottom wall normalized by U_∞ and iso-surface of the fluid pressure coefficient $c_p = (p - p_\infty)/(\rho_{\text{air}}\, U_\infty^2/2) = -0.48$).

et al. (2018), but clearly visible in the PSDs of the measurements. The symmetric vortex shedding is clearly detectable at St = 0.27 for Re = 50,000, around St = 0.28 for Re = 75,000 and at St = 0.26 for Re = 100,000. These values are also in good agreement with the experimental data ($\text{St}_{\text{exp}} = 0.27$ for Re = 50,000, $\text{St}_{\text{exp}} = 0.29$ for Re = 75,000 and $\text{St}_{\text{exp}} = 0.28$ for Re = 100,000).

In the PSDs of Fig. 13 remarkable frequencies are also noticed around St = 0.22, St = 0.25 and St = 0.33. These frequencies derive from the random alternation in time of the previously mentioned shedding types. An example of the vortex shedding occurring at the sides of the hemisphere near the wall is schematically sketched in Fig. 14(e): One second of real time is presented: One complete von Kármán shedding cycle occurs at its nominal frequency of 5.5 Hz temporally embedded by symmetrically shed vortices corresponding to a nominal frequency of 9.2 Hz. By counting the vortices shed in one second, an intermediate frequency of about 8.5 Hz is found corresponding to St = 0.25 for the case Re = 50,000. As the alternation in time of both shedding types is random, other intermediate Strouhal numbers between St = 0.16 and St = 0.27 can appear such as St = 0.22.

Additional frequencies are present at a Strouhal number around St = 0.40 for Re = 50,000, around St = 0.37 for Re = 75,000 and around St = 0.40 for Re = 100,000. Similar values are found in the measurements. They are particularly strong in the recirculation at the points E30, E45 and E60. No shedding of vortices are observed at this particular frequency for a given Re. Therefore, contrary to Wood et al. (2018), these Strouhal numbers cannot be linked to roll-up vortices.

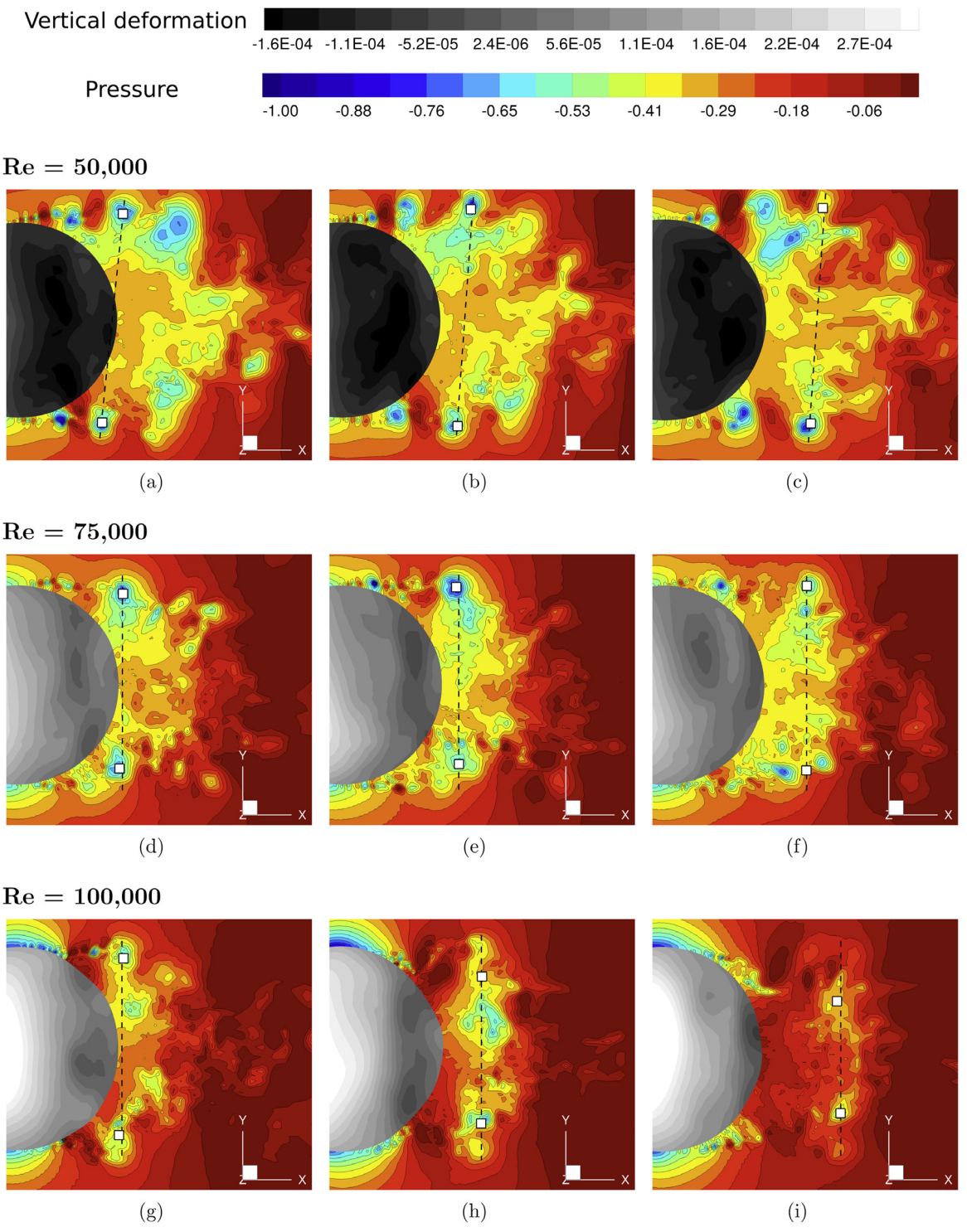

Fig. 17. Visualization of the instantaneous vertical deformations normalized by $U_\infty^2/(2g)$ and of the vortical structures (fluid pressure coefficient $c_p = (p - p_\infty)/(\rho_{\text{air}}\, U_\infty^2/2)$ near the bottom wall) at the back of the flexible hemisphere in case of the symmetric shedding type for three instants in time; symmetric arc-type vortices are highlighted by square symbols.

Nevertheless, they are connected to the flow and not to the structure, since the same frequencies are observed in the measurements and in the simulations involving the rigid hemisphere.

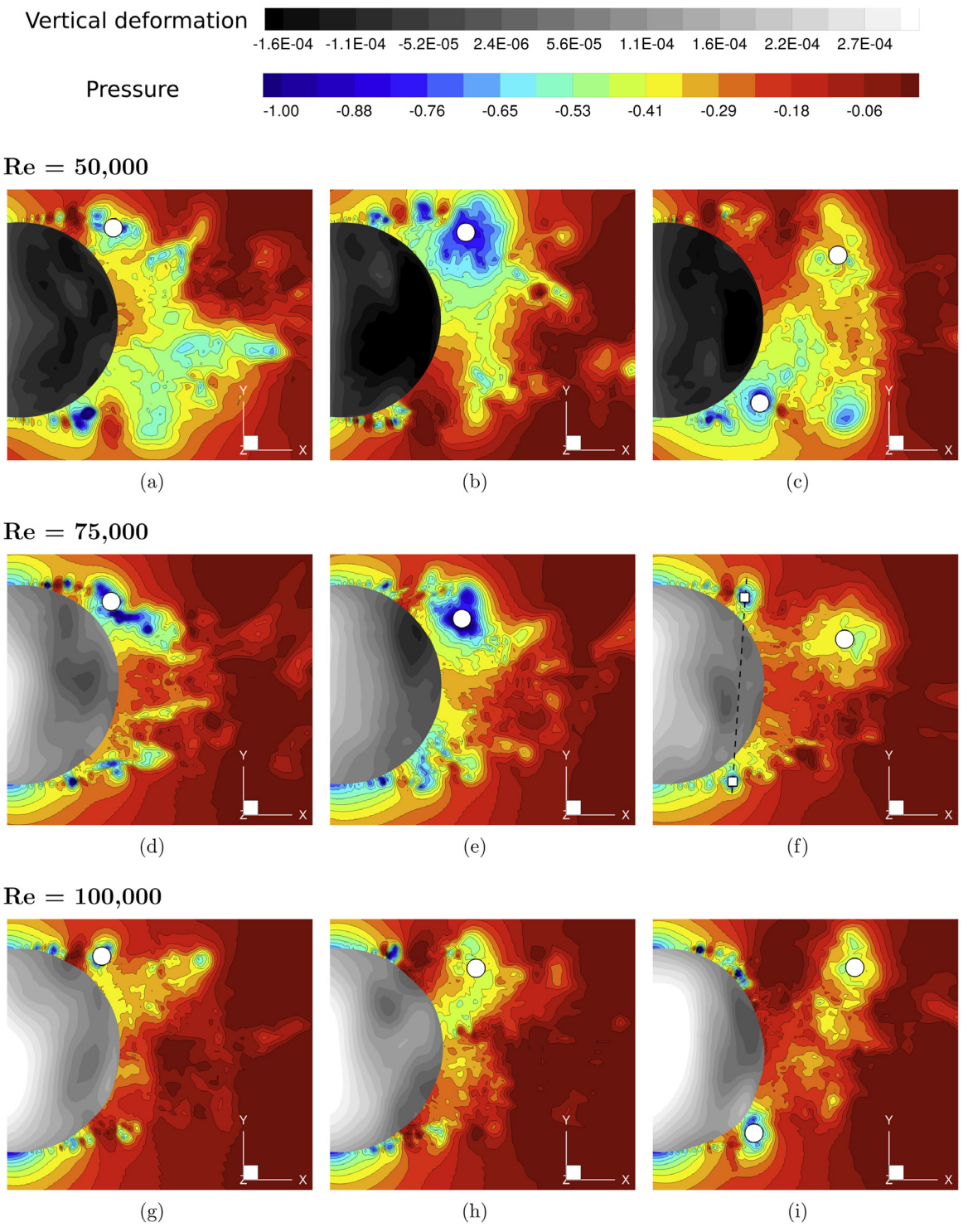

Fig. 18. Visualization of the instantaneous vertical deformations normalized by $U_\infty^2/(2g)$ and of the vortical structures (fluid pressure coefficient $c_p = (p - p_\infty)/(\rho_{\text{air}}\, U_\infty^2/2)$ near the bottom wall) at the back of the flexible hemisphere in case of the alternating shedding type for three instants in time; symmetric arc-type vortices and von Kármán vortices are highlighted by square and circle symbols, respectively.

The previously mentioned large-scale symmetric and von Kármán vortices do not directly form on the separation line on the membrane, but beyond at about $x/D \approx 0.5$. In the free shear layer close to the separation line small vortices detach

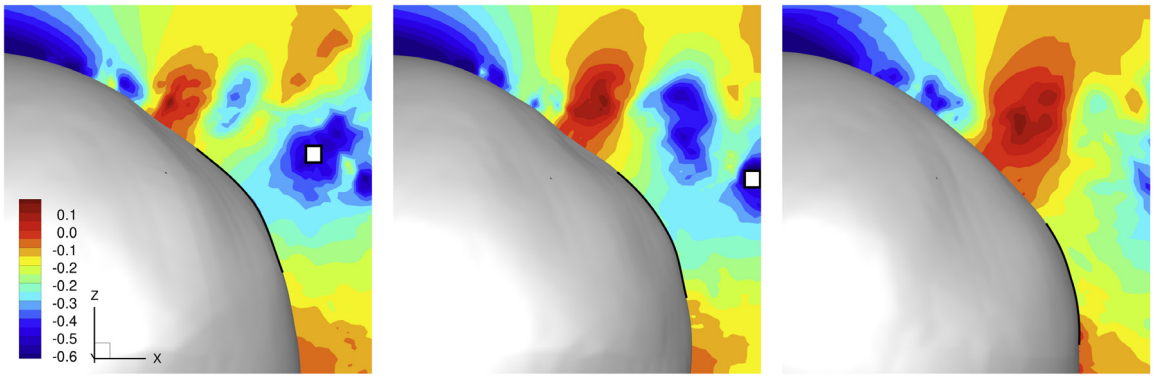

(a) t_0. (b) t_1. (c) t_2.

Fig. 19. Deformations induced by the shedding of a symmetric arc-type vortex marked with a square symbol (Re = 100,000; fluid pressure coefficient $c_p = (p - p_\infty)/(\rho_{\text{air}}\, U_\infty^2/2)$ at $y = 0$; Deformation magnified by a factor of 3).

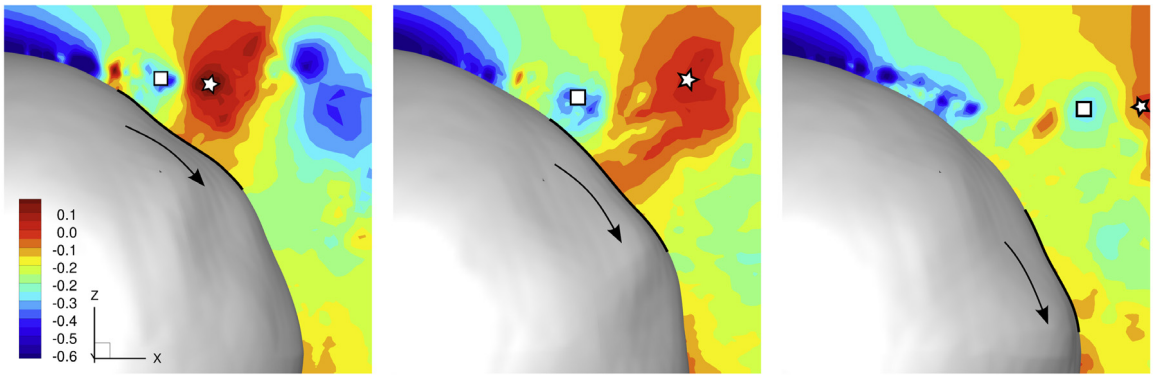

(a) t_0. (b) t_1. (c) t_2.

Fig. 20. Wave of deformations induced by the formation and shedding of medium-scale vortices on the top of the hemisphere (Re = 100,000; fluid pressure coefficient $c_p = (p - p_\infty)/(\rho_{\text{air}}\, U_\infty^2/2)$ at $y = 0$; Deformation magnified by a factor of 3).

at very high frequencies due to Kelvin–Helmholtz instability. These are too weak to imply a significant deformation of the flexible structure. Considering the upper part of the structure these small vortical structures merge to result in medium-sized vortices at about $x/D \approx 0.25$, which move downwards quasi parallel to the ground at a Strouhal number around 1.5 (see Fig. 20). Note that these medium vortices are not the symmetric arc-type or von Kármán vortices. The formation of these medium-scale structures induces an additional deformation of the membrane in form of a wave. Fig. 20 shows that the core of these medium vortices (marked by a square symbol), corresponding to negative pressure, results in a suction of the membrane. Contrarily, between two vortices, the area of high pressure (marked by a star in the figures) leads to a small indentation. The shedding of vortices implies a movement in the wave, which travels downwards on the rear side of the flexible structure. It hits the bottom and partially reflects back towards the apex of the hemisphere. This FSI phenomenon is not mentioned in the experimental paper of Wood et al. (2018). In order to identify it, coupled fluid and structure results relying on a high temporal and spatial resolution such as available by the predictions are required, as well as the pressure distribution and the possibility to artificially amplify the resulting deformations.

Table 3 summarizes the predicted FSI frequencies which can be directly correlated to the fluid motion and compares them with the measurements of Wood et al. (2018).

5.3.2. FSI frequencies related to the structure

It is assumed that the dominant frequencies related to the structure in the PSD data originate from its modal response characteristics, i.e., the natural eigenfrequencies of the hemisphere. In this case these frequencies should not change with increasing Reynolds number. Thus, their physical values are plotted and not an associated St number, which would change with Re. Based on this assumption the following FSI frequencies are related to the structure:

- At about **29 Hz** a large peak is present for all Re corresponding to the first two eigenmodes of the hemispherical membrane as depicted in Fig. A.28(a). The first eigenmode is a translational displacement of the membrane in the

Table 3
Comparison of the predicted FSI Strouhal numbers resulting from the fluid motion with the corresponding data based on the measurements of Wood et al. (2018). The symbol ✌ corresponds to a value similar to the predicted one and visible in the PSDs of the measurements, but not mentioned in the experimental paper.

		Re = 50,000		Re = 75,000		Re = 100,000	
		Sim.	Exp.	Sim.	Exp.	Sim.	Exp.
von Kármán vortex shedding	lateral force	0.08	✌	0.085	✌	0.08	✌
von Kármán vortex shedding	drag force	0.16	0.16	0.17	0.17	0.16	0.17
symmetric vortex shedding		0.27	0.27	0.28	0.29	0.26	0.28
flow excitation in recirculation		0.40	0.40	0.37	0.37	0.40	0.44
medium-sized vortex shedding		1.45	✌	1.52	✌	1.55	✌

streamwise direction, whereas the second is a translational displacement in the transversal direction. Note that for Re = 100,000 it also corresponds to St = 0.44.

- A frequency of about **42 Hz** coincides with the third structural eigenmode (denoted f_n^2 in Wood et al. (2018), which is mainly a translation in the vertical direction (see Fig. A.28(b)). It is also noticed in the experimental PSD data of Wood et al. (2018).
- Between **50–53** Hz several thin but strong peaks are detectable. As shown by the modal analysis of Appendix A.3 four eigenmodes (4th, 5th, 6th and 7th) are present in this range. These eigenmodes are more complicated and composed of local radial expansions and contractions.
- Around **60 Hz** remarkable peaks are detected similar to the measurements. In the linear modal analysis the eigenmodes between the 8th and 17th are computed around this value. They contain more local expansions and contractions in the radial direction than the previous ones. The eigenfrequency f_n^3 was reported at 62 Hz in Wood et al. (2018). As shown with the structure test case of Appendix A.2, frequencies around 60 Hz play a major role in the dynamic deformation response of the current model.
- Around **70**, **80** and **90 Hz** sharp peaks are also present for quasi all deformation components and for all Reynolds numbers in the current PSD data. These frequencies were also noticed in the experimental PSD ones. Around these values, several eigenmodes found by the linear modal analysis of Appendix A.2 can be linked to the experimental ones reported in Wood et al. (2018) ($f_n^{4,5,6,7,8}$). These alternate between several modes with local expansions and contractions in the radial direction and one mode with a dominant deformation in vertical direction. The higher the eigenfrequency, the higher is the expansion–contraction number.

6. Conclusions

The current contribution presents the numerical counterpart of the experimental fluid–structure interaction study of Wood et al. (2018) on an air-inflated thin-walled flexible membranous hemisphere exposed to a turbulent boundary layer. Three different cases corresponding to three Reynolds numbers (Re = 50,000, 75,000 and 100,000) are investigated with the help of a FSI framework especially developed for membrane structures within turbulent flows (Breuer et al., 2012). In order to solve the coupled problem, a partitioned method is applied. The large-eddy simulation technique relying on a finite-volume discretization is used for the fluid side. The flexible membrane structure is modeled based on a standard finite-element model taking large deformations into account. The material (silicone) used in the experiments is described by the St. Venant–Kirchhoff material model. The correct initial hemispherical shape is reached applying a constant pre-stress. The inherent material damping is reproduced based on the Rayleigh damping with damping parameters derived from the experiments. For the current configurations a loose coupling algorithm is sufficient and permits a significant reduction of the CPU-time requirement.

First, the conclusions obtained separately for the pure fluid simulations and for the pure structure tests are summarized. For the fluid, the simulations relying on the rigid hemisphere show a very good agreement with the experiment concerning the synthetic turbulent inlet data (see De Nayer et al., 2018). Moreover, at Re = 50,000, the time-averaged first- and second-order moments of the flow field coincide very well with the experimental reference of Wood et al. (2016). At higher Re some deviations to the experimental data appear in the wake due to the relatively coarse resolution of the grid with increasing distance from the structure. Nevertheless, the trends predicted by LES are similar to the experimental ones. For the structure model, a quasi perfect fit is obtained for the static behavior of the membrane combining the St. Venant–Kirchhoff material parameters given by the experiments with a constant initial pre-stress. The dynamic deformation response of the membrane is in accordance with the reference applying a Rayleigh damping derived from the experimental data. The eigenfrequencies

of this deformation also correspond well. However, the dominant eigenmodes are different. Nevertheless, the modeling of both domains is sufficiently accurate to be used in the coupled FSI simulations.

The FSI results rely on simulations for a dimensionless time interval of $t^* \geq 200$ to have enough data for the time-averaging and to study the complex instantaneous FSI phenomena. The comparison of the time-averaged first- and second-order moments with the experiments show similar trends, but deviations appear in the wake similar to the rigid case. The time-averaged deformations are in good agreement with the experimental data for all three Re considered. Owing to very small interface velocities and low Reynolds stresses found on the FSI interface, the time-averaged deformed shape of the structure seems to have more impact on the changes observed between the flow fields of the rigid and the flexible hemisphere than the fluctuations of the displacements. Concerning the standard deviations of the membrane deformation the same order of magnitude is observed in the simulations and the experiments. In the vertical direction, the distribution of the standard deviations obviously differs. This can be attributed to differences in the dominant eigenmodes of the numerical structure model. Despite these minor discrepancies an overall satisfying agreement is reached by the simulations. Thus, the results can be used to characterize the transient FSI phenomena.

The FSI phenomena observed in the current cases can be classified into two categories depending on whether they are related to the fluid or to the structure.

The FSI frequencies related to the fluid are linked to different types of remarkable vortex sheddings, which are explained in detail. Large vortical structures are shed near the ground from the side of the body in an alternate von Kármán manner at St $\approx$ 0.16, which is in perfect agreement with the experiment. They induce strong and asymmetric deformations on the rear side of the body. As the shedding is asymmetric, a second Strouhal number, half of the above-mentioned, is also noticed at St $\approx$ 0.08. The von Kármán pattern alternates with another remarkable shedding type: An arc-type symmetric vortical structure forms behind the bluff body and detaches at a Strouhal number of about 0.27 also found in the experiment of Wood et al. (2018). It implies a suction with a low pressure region and therefore a short-term symmetric expansion of the rear side of membrane. Both shedding types are not simultaneously found in the flow. The random alternation of both types generates combined FSI Strouhal numbers between 0.08 and 0.27. The shedding processes of these large vortices do not occur at the separation line, but at the beginning of the recirculation region. At the separation line a detachment of small vortices at very high frequencies is present. Their low energy content does not directly produce any significant membrane deformations. However, due to the Kelvin–Helmholtz shear layer instability, the small vortices merge in the shear layer forming medium-sized vortices with a Strouhal number of about 1.5 moving downstream. The succession of negative and positive pressure fluctuations induces a series of indentations and elevations on the membrane. Due to the downward movement of the vortices a wave of deformations is generated on the rear side. This phenomenon could not be found during the postprocessing of the experimental results (Wood et al., 2018), since no pressure fields were available and no simultaneous acquisition of fluid and structure data was possible. Additionally, a flow excitation in the recirculation region is noticed at about St $\approx$ 0.40. A similar value is observed in the measurements data. However, contrary to Wood et al. (2018), it seems not to be linked to the roll-up vortices. Nevertheless, the corresponding phenomenon is flow related, since this Strouhal number is also present in the case involving the rigid hemisphere.

The FSI frequencies related to the structure are linked to the corresponding eigenmodes of the finite-element model of the hemispherical membrane. The first and second eigenmodes around 30 Hz, corresponding to the streamwise and spanwise translational movement of the structure, are strongly present in the response of the FSI simulation. These eigenfrequencies are visible in the experimental data, but were not explained in Wood et al. (2018). The third eigenmode at about 42 Hz, also noticed in the experiment, plays a major role particularly in the vertical FSI response, since this eigenmode corresponds to a vertical expansion of the model. The next eigenmodes are a succession of local expansions and indentations of the membrane. The number of local extrema increases with the eigenfrequency. Remarkable peaks around 60, 70, 80 and 90 Hz are found in the FSI simulations and linked to the corresponding experimental and numerical eigenfrequencies.

The air-inflated flexible hemisphere exposed to a turbulent boundary layer is a challenging FSI case from both points of view, the experimental investigation and the numerical simulation. Table 4 lists the advantages and drawbacks observed for both experimental and numerical approaches during the investigations. Obviously, the respective pros and cons are typically of complementary nature, which therefore substantiates the great potentials for getting deep insights into complex FSI phenomena by thoroughly planned concurrent experiments and high-fidelity simulations for a specific FSI scenario.

Acknowledgments

The authors thank W. Warnecke (Professur für Strömungsmechanik, Helmut-Schmidt-Universität Hamburg, Germany), F. Pean, A. Ghantasala and B. Philipp (Lehrstuhl für Statik, Technische Universität München, Germany) for their contributions to this work. The project is financially supported by the *Deutsche Forschungsgemeinschaft* under the contract numbers BR 1847/12-2 and BL 306/26-2. The computations were partially carried out on the German Federal Top-Level Computer SuperMUC at LRZ Munich under the project numbers `pr84na` and `pr53ne`.

Appendix. Evaluation of the structure model

A.1. Steady calibration case: Flexible hemisphere with variable inner pressure

The steady CSD calibration case explained in detail by Wood et al. (2018) is computed using the setup described in Section 4.2 in order to validate the material parameters and to calibrate the pre-stress tensor $\mathbf{n}_0$ necessary for the membrane

Table 4
Summary of the advantages and drawbacks encountered for both experimental and numerical approaches for the present FSI problem.

Experiments (Wood et al., 2018)	Present FSI simulations
✓ possibility to get large datasets of a long time span (very accurate frequency analysis)	✓ higher temporal and spatial resolution, but for a limited time span
✓ possibility to quickly rearrange the experiment to investigate different parameters	✓ simultaneous 3D fluid and structure data due to full FSI simulation
✗ non-simultaneous acquisition of the fluid and structure data	✓ velocity and pressure fields available for the fluid
✗ DIC 3D-measurement restricted to a correlation overlap area in the stereo setup	✗ huge CPU-time requirements for one FSI simulation, therefore limited parameter studies
✗ only velocity data available for the fluid	✗ very long post-processing due to the amount of 3D data
✗ only 2D fluid fields available for the present setup	✗ difficulty to perfectly model the material and to represent the temporal and spatial behavior observed in the experiments

model. The correct specification of the pre-stress distribution is of high importance, since it is a very decisive parameter of the inflated membrane structure, which is in stable equilibrium before it is subjected to the flow field. Thus, the structural response in the coupled FSI case is strongly depending on the pre-stress state.

The components of the pre-stress tensor $\mathbf{n}_0$ are defined in a local Cartesian coordinate system on the surface of the membrane. Here, the normal components of the pre-stress tensor are assumed to be constant and equal to n_{membrane}, while the shear component is considered to be negligible. Note that n_{membrane} is not given by the experiments. In the experiment the inflated structure maintains a perfect hemispherical shape when a pressure difference of $\Delta p_{\text{cal}} = 43$ Pa is applied. Thus, a first approximation of n_{membrane} is achieved using the 2D Barlow's formula (DIN 2413) given by $n_{\text{membrane}} = \Delta p_{\text{cal}}\, D/(4\, t_{\text{membrane}})$. Applying Barlow's formula with an averaged thickness of the membrane[7] $t_{\text{membrane}} = 1.65 \times 10^{-4}$ m leads to a pre-stress value of $n_{\text{membrane}} = 9772.7$ Pa. In a simulation applying this pre-stress value and the pressure difference of $\Delta p_{\text{cal}} = 43$ Pa, the membrane structure is in equilibrium and stays in a hemispherical shape (see Fig. A.22). However, Barlow's formula does not take the gravitational force into account. Since the gravitational force cannot be neglected in the present case, the value of the pre-stress n_{membrane} has to be slightly re-adjusted in an iterative manner.

In the experimental setup, the pressure difference Δp was varied and the z-component of the resulting displacement was measured at the apex of the hemisphere. Similar to the experiment, different values of the pressure load are applied on the membrane in the simulation and the z-component of the displacement at the apex of the hemisphere is determined. For this purpose, the Young's modulus is set to the experimental value $E_{\text{silicone}} = 7 \times 10^5$ Pa determined by the tensile test (according to EN ISO 527–2, see Wood et al., 2018).

For the finite-element discretization the *Constant Strain Triangle* (CST) element is used (Hughes, 2012). Four levels of refinement of the grid are applied, 360 elements, 908 elements, 1926 and 4080 elements, respectively (see Fig. A.21).

For these four grids and the material parameters mentioned above, simulations are conducted setting the pre-stress value as a first guess according to Barlow's formula to $n_{\text{membrane}} = 9772.7$ Pa. These investigations are done with and without considering the gravitational forces. The vertical displacements obtained at the monitoring point $\text{P}_{\text{apex}}\,(0, 0, D/2)$ are summarized and compared with the measurements in Fig. A.22. As expected the results for the case without gravitational force show that the pre-stress based on Barlow's formula leads to a close coincidence between predictions and measurements and thus gives a satisfying evaluation of the pre-stress. For the case with gravitation a perfect fit with the measurements is achieved by an adjusted pre-stress of $n_{\text{membrane}} = 7794.5$ Pa. Thus, this value is used in the rest of the investigation. Comparing the results of the different grid refinement levels, the mesh with 360 elements proves to be too coarse and thus is no longer considered. The results relying on the meshes with either 1926 or 4080 elements differ very slightly, nicely showing that the solution with the 1926 elements mesh is already converged. The present structure model of the flexible membrane is therefore able to reproduce the behavior observed in the steady calibration case of Wood et al. (2018).

A.2. Unsteady case: Response of the flexible hemisphere to an excitation

The transient response of structures is influenced by the inherent material damping. Thus, it has to be modeled appropriately in order to achieve a good agreement with the experimental results. Within this contribution, the structural damping is modeled by the so-called Rayleigh damping. The finite-element damping matrix is computed as a linear combination of the mass matrix $\mathbf{M}$ and the linearized stiffness matrix $\mathbf{K}$:

$$\mathbf{D} = \alpha\, \mathbf{M} + \beta\, \mathbf{K}\,. \tag{A.1}$$

[7] Based on the given material properties and the perfect hemispherical geometry, the mass of the membrane is computed to $m^{\text{theory}}_{\text{membrane}} = 1/12\,\pi\,(D^3 - (D - 2\,t_{\text{membrane}})^3)\,\rho_{\text{silicone}} \approx 6.11 \times 10^{-3}$ kg. Compared to the averaged mass of the experimental models $m^{\text{exp}}_{\text{membrane}} = 6.22 \times 10^{-3}$ kg, the error is low (1.8%).

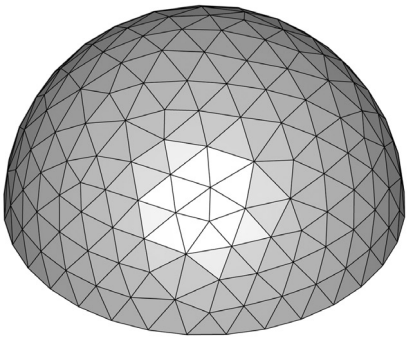

(a) Mesh with 360 elements.

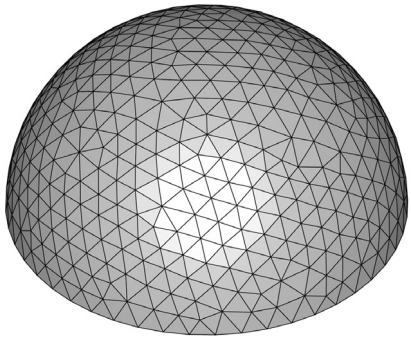

(b) Mesh with 908 elements.

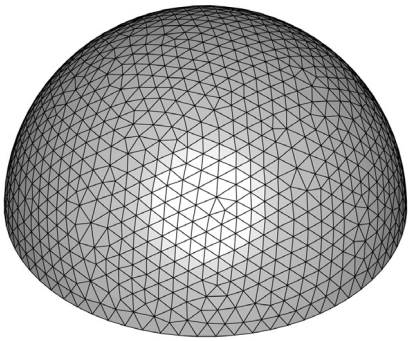

(c) Mesh with 1926 elements.

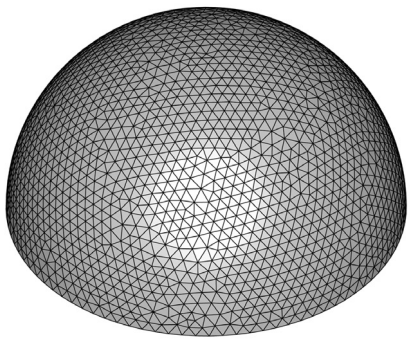

(d) Mesh with 4080 elements.

Fig. A.21. Finite-element discretization of the membranous flexible structure.

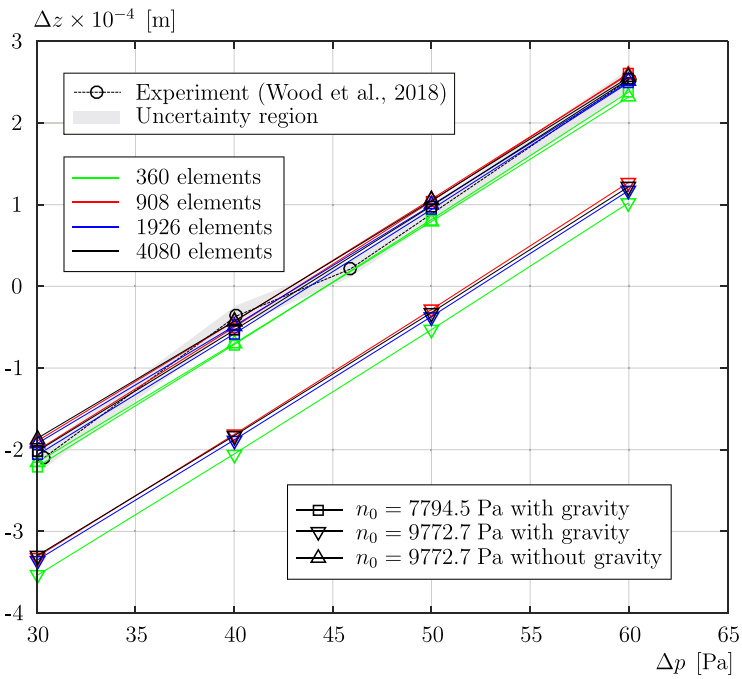

Fig. A.22. Steady calibration case: z-displacement at the apex of the hemisphere as a function of Δp for the numerical models in comparison with the experimental values.

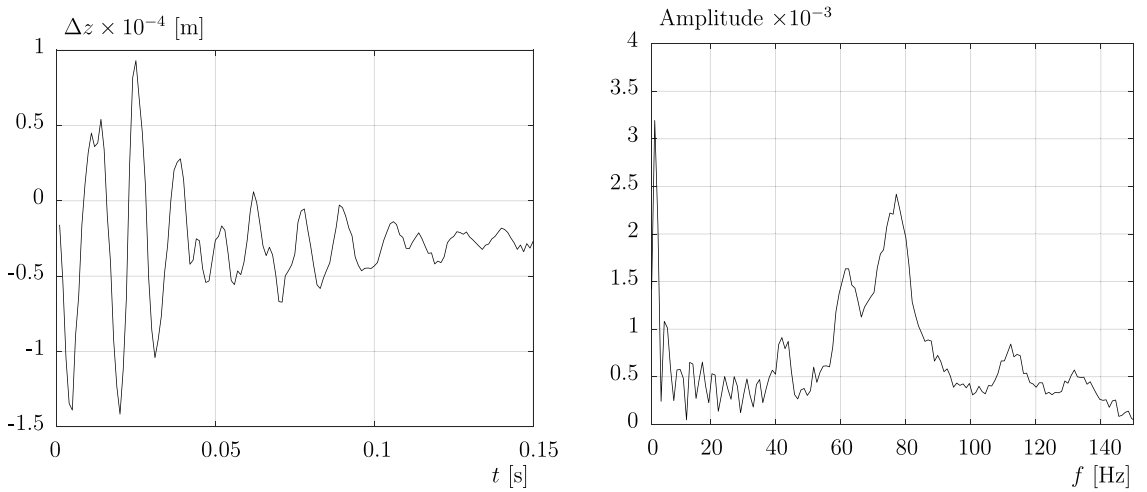

(a) Response in physical space. (b) Response in frequency space.

Fig. A.23. Unsteady case: Experimental response of the apex of the hemisphere.

The parameters α and β stand for the Rayleigh damping parameters which have to be determined. Following Chowdhury and Dasgupta (2003) the Rayleigh damping parameters can be estimated based on two significant eigenfrequencies of the structure f_i and f_j and their corresponding damping ratios ζ_i and ζ_j as follows

$$\alpha = \frac{2\omega_i\,\omega_j}{\omega_j^2 - \omega_i^2}\left(\omega_j\zeta_i - \omega_i\zeta_j\right) , \tag{A.2a}$$

$$\beta = \frac{2\omega_i\,\omega_j}{\omega_j^2 - \omega_i^2}\left(\frac{\zeta_i}{\omega_j} - \frac{\zeta_j}{\omega_i}\right) , \tag{A.2b}$$

where $\omega_i = 2\pi f_i$ and $\omega_j = 2\pi f_j$ denote the corresponding angular frequencies of the eigenfrequencies f_i and f_j, respectively.

To determine the two relevant eigenfrequencies of the structure f_i and f_j and their corresponding damping ratios, the response of the membrane (i.e., the vertical displacement Δz) to an local excitation measured in the experiments of Wood et al. (2018) is used (see Fig. A.23(a)). The response in the frequency domain is obtained by a discrete Fourier transformation depicted in Fig. A.23(b). Both figures are focusing only on the time and frequency ranges of interest.

Based on Fig. A.23(b) two significant frequencies are chosen: the first remarkable frequency $f_i = 42$ Hz and the frequency with the largest amplitude $f_j = 78$ Hz. For both frequencies two rectangular windows w_i and w_j are constructed in the frequency space, respectively, as follows,

$$w_i(f) = \begin{cases} 1 & \text{, if } 37 \text{ Hz} \leq f \leq 46 \text{ Hz} \\ 0 & \text{, else ,} \end{cases} \tag{A.3a}$$

$$w_j(f) = \begin{cases} 1 & \text{, if } 67 \text{ Hz} \leq f \leq 96 \text{ Hz} \\ 0 & \text{, else .} \end{cases} \tag{A.3b}$$

The windows w_i and w_j are Heaviside step-type functions rather than Dirac delta functions because the frequency spectrum of the experiment is continuous (see Fig. A.24(a) and (c)). The widths of the windows w_i and w_j are chosen such that the corresponding responses[8] in physical space show an exponential decay as theoretically expected. The filtered responses of the extracted frequencies f_i and f_j in physical space are depicted in Fig. A.24(b) and (d), respectively.

Subsequently, the logarithmic decrement, Λ_i and Λ_j for each frequency f_i and f_j is computed by

$$\Lambda = \frac{1}{n}\log\frac{\Delta z(t)}{\Delta z(t+nT)} , \tag{A.4}$$

where T stands for the period of the oscillations and n for the number of periods between the two peaks $\Delta z(t)$ and $\Delta z(t+nT)$. In addition, the predicted exponential decay is shown in red. Using Eq. (A.4) the logarithmic decrements for frequency f_i and

[8] By a convolution of each window with the response in the frequency space, the corresponding response of the filtered eigenfrequency in the physical space is recovered using an inverse discrete Fourier transformation.

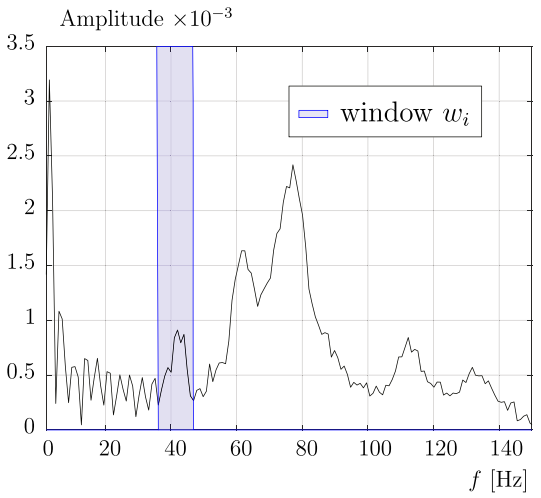

(a) Window for frequency f_i.

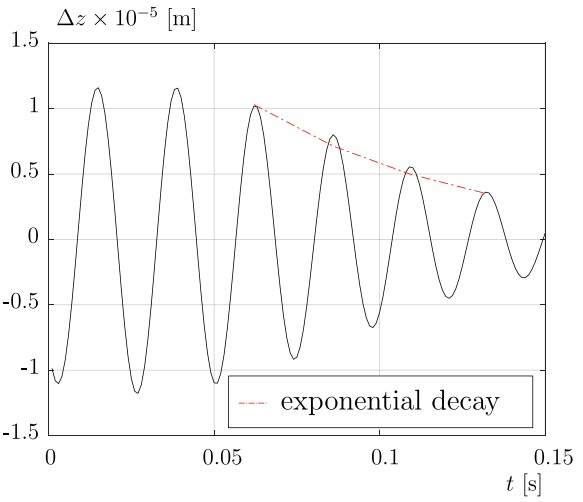

(b) Response of frequency f_i in physical space.

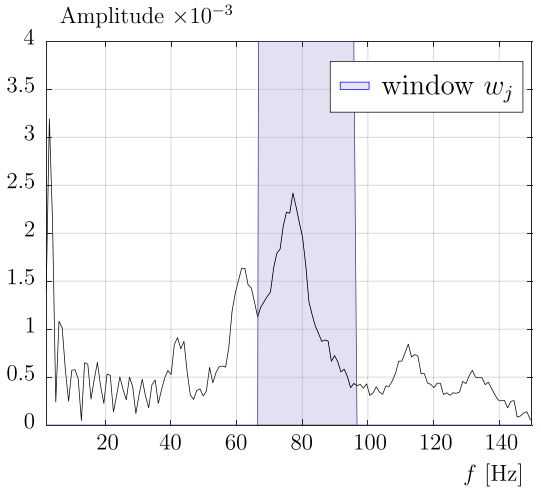

(c) Window for frequency f_j.

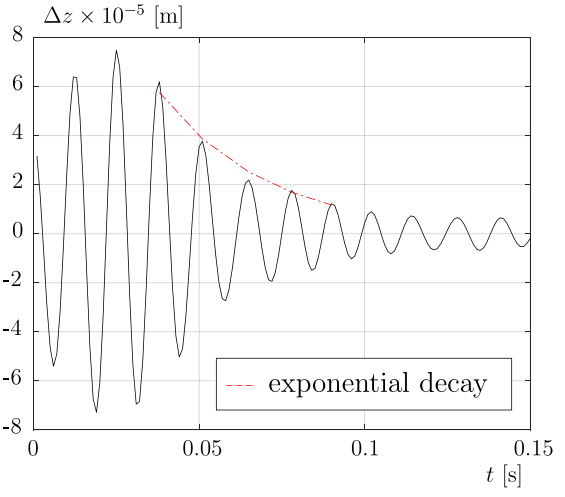

(d) Response of frequency f_j in physical space.

Fig. A.24. Response of the apex of the hemisphere corresponding to frequencies $f_i = 42$ Hz and $f_j = 78$ Hz.

f_j are determined using Fig. A.24(b) and (d) as $\Lambda_i = 0.366$ and $\Lambda_j = 0.405$. The damping ratio ζ is then given as a function of the logarithmic decrement Λ as

$$\zeta = \frac{\Lambda}{\sqrt{4\pi^2 + \Lambda^2}}\,, \tag{A.5}$$

which leads to $\zeta_i = 0.058$ and $\zeta_j = 0.064$. Substituting these damping ratios into Eq. (A.2) yields the following Rayleigh damping parameters $\alpha = 17.47$ and $\beta = 1.89 \times 10^{-4}$.

In order to evaluate these Rayleigh damping parameters, the transient case of the response of the hemisphere to an excitation presented by Wood et al. (2018) is now simulated with FEM. Herein, the hemisphere is exposed to a point load $\mathbf{F}(t) = -F(t)\left(\frac{\sqrt{2}}{2}\mathbf{e_x} + \frac{\sqrt{2}}{2}\mathbf{e_z}\right)$, for which the amplitude is defined by

$$F(t) = \begin{cases} 0.018 \text{ N}, & t < 0.001 \text{ s}, \\ 0, & \text{else}. \end{cases} \tag{A.6}$$

This amplitude value is chosen to get an initial local deformation of the membrane similar to the experiment. The point load is applied at an angle $\phi = \frac{\pi}{4}$ at the meridian direction in the x–z-plane, see Fig. A.25. As it can be deduced from Eq. (A.6) the aforementioned load is a Heaviside step-type load in time. As in the experiment the pressure difference Δp is set to 43 Pa. The FEM simulation takes the gravitational force into account and applied the adjusted pre-stress of $n_{\text{membrane}} = 7794.5$ Pa

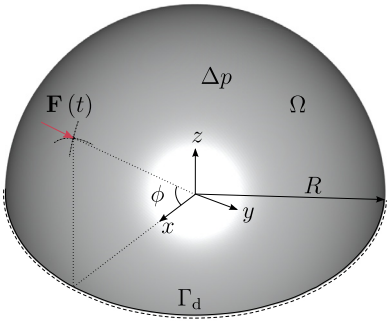

Fig. A.25. Problem setup for the hemispherical pressurized membrane.

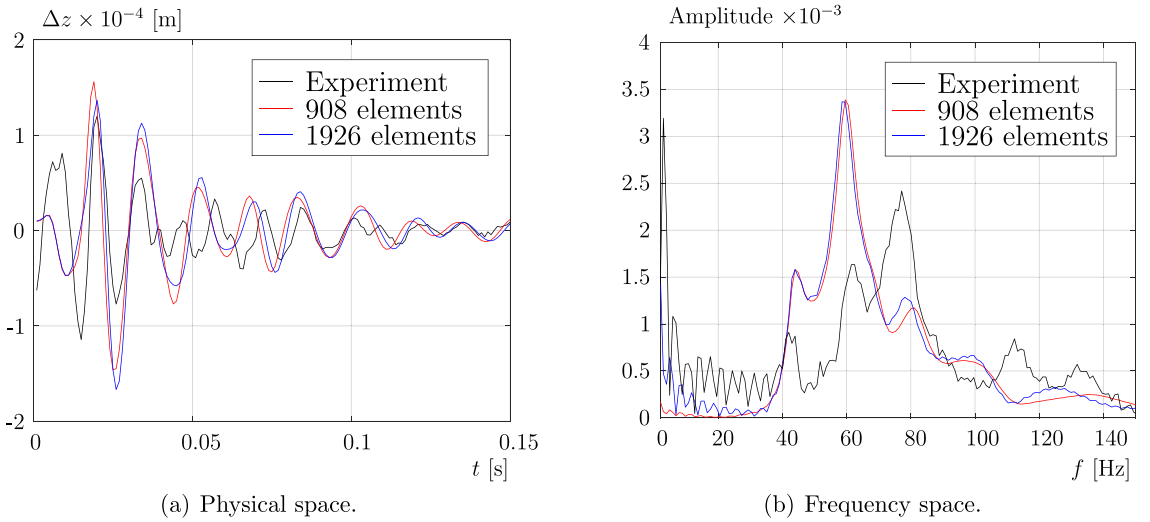

(a) Physical space. (b) Frequency space.

Fig. A.26. Unsteady case: Comparison of the simulation results with the experimental data.

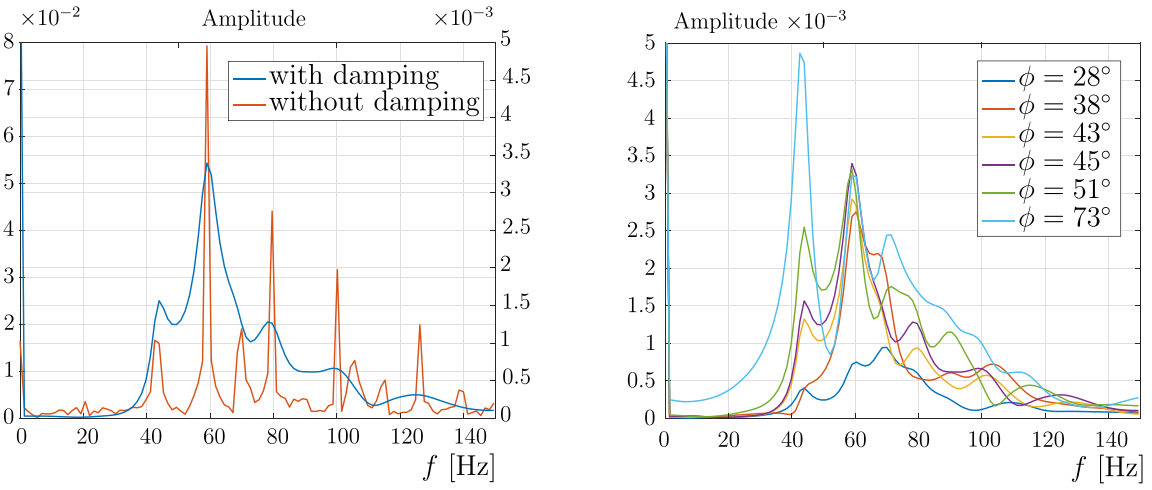

(a) Influence of the Rayleigh damping. (b) Influence of the point-load excitation angle.

Fig. A.27. Unsteady case: Predicted deformations in frequency space for slightly different configurations.

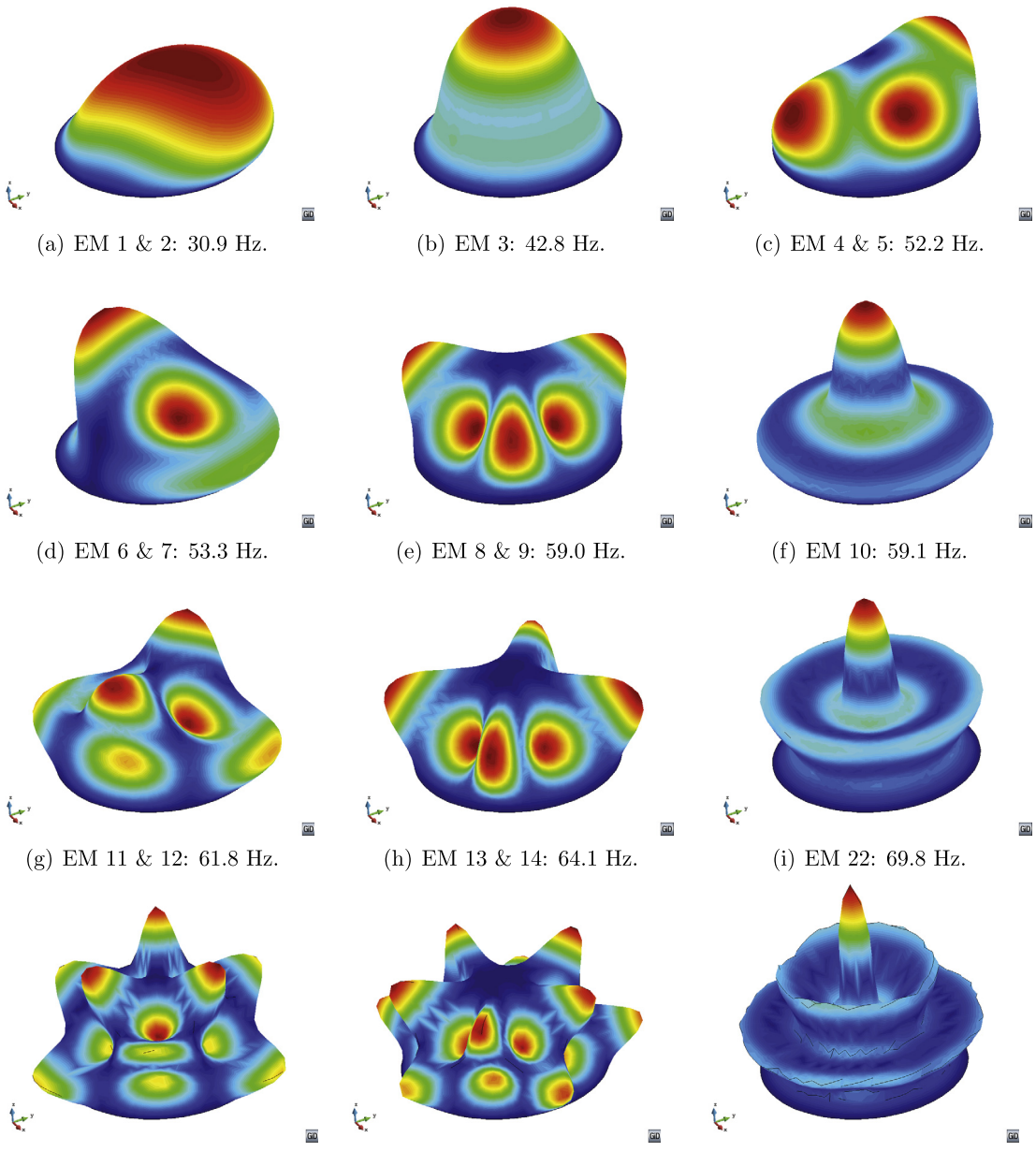

(a) EM 1 & 2: 30.9 Hz. (b) EM 3: 42.8 Hz. (c) EM 4 & 5: 52.2 Hz.

(d) EM 6 & 7: 53.3 Hz. (e) EM 8 & 9: 59.0 Hz. (f) EM 10: 59.1 Hz.

(g) EM 11 & 12: 61.8 Hz. (h) EM 13 & 14: 64.1 Hz. (i) EM 22: 69.8 Hz.

(j) EM 31 & 32: 77.4 Hz. (k) EM 33 & 34: 78.8 Hz. (l) EM 56: 91.9 Hz.

Fig. A.28. Modal analysis: Selected eigenmodes (EM) with corresponding eigenfrequencies.

found in Appendix A.1. Since the ratio of the structure density to the fluid density is large ($\rho_{\text{silicone}}/\rho_{\text{air}} \approx 857$), the fluid at rest around the flexible structure has a minimal impact on the problem and is neglected here.

Applying the previously determined Rayleigh damping parameters in combination with the structural parameters given in Section 3.1, the transient case is simulated on the grid with either 908 or 1926 elements. For the time integration, the classical Newmark method is employed with a time step size of $\Delta t = 10^{-3}$ s. The results of the simulations are compared with the measurements (see Fig. A.26) demonstrating a good accordance concerning the damping behavior between the experimental and the numerical results for both grids. Therefore, these damping parameters are used for the FSI simulations. The striking frequencies 42 Hz, 62 Hz and 78 Hz are visible in the frequency space of the simulations and the experiments. However, in the simulations the frequency 62 Hz predominates instead of 78 Hz observed in the experiments meaning that the structural eigenmodes with an eigenfrequency around this value will play a major role in the deformation of the whole membrane.

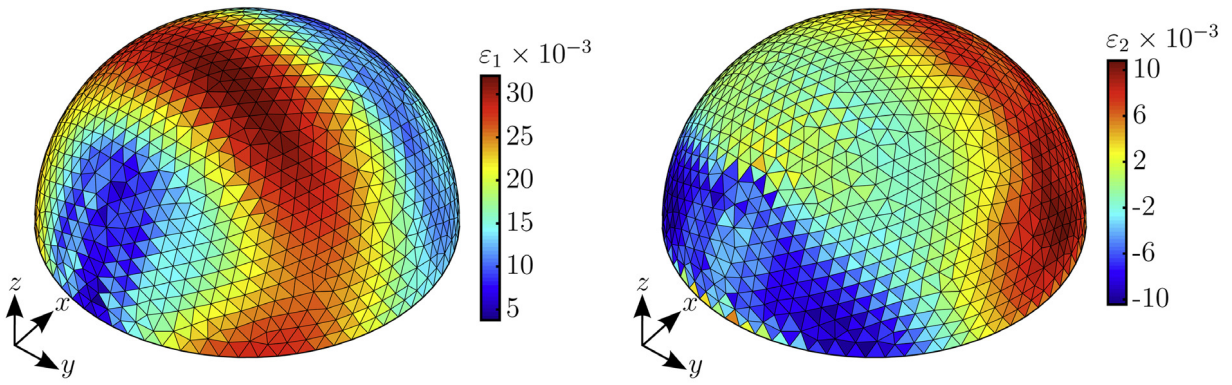

(a) ε_1. (b) ε_2.

Fig. A.29. Principal strain contours at time instances where the maxima occur (case Re = 100,000).

In order to better apprehend this result, the current test case is re-run with slightly different computational setups. In a first step, two simulations with the original excitation, i.e., the point load **F** at $\phi = 45°$, with and without Rayleigh damping are compared in Fig. A.27(a). It is seen that the Rayleigh damping does not affect the arrangement of the predominant modes. The mode at 62 Hz dominates the others independent of the damping. In a second step, the point load **F** is applied at different angles ϕ for a simulation with Rayleigh damping and the dynamic response in the frequency space is compared in Fig. A.27(b). The excitation angle has a significant impact on the order of the predominant modes. With increasing ϕ the mode at 42 Hz (EM 3) becomes stronger and even dominates for $\phi = 73°$. Is it also interesting to notice that the amplitude of the mode around 60 Hz is nearly constant for $\phi > 28°$. A peak between 70 and 80 Hz is also present similar to the experiments, however with a lower amplitude.

In summary, the structure model of the flexible membrane is also able to reproduce the behavior of the dynamic experimental case of Wood et al. (2018) with a correct amplitude of the deformation and with an acceptable representation of the eigenfrequencies. However, the dominant eigenmode in the dynamic response of the present structure model will be around 60 Hz instead of between 70 and 80 Hz as in the experiments.

A.3. Modal analysis

A modal analysis is conducted applying the structure solver Carat++ and the CSD setup described in Section 4.2. It is performed for the membrane with the inner pressure of 43 Pa, for which the hemispherical shape is maintained. The tangent stiffness matrix of the geometrically non-linear problem obtained after a static analysis is used for the eigenvalue problem. In this way, the developed internal stresses due to the stabilization of the membrane by the internal pressure are taken into consideration within the modal analysis. As mentioned before, the ratio of the structure density to the fluid density is large ($\rho_{\text{silicone}}/\rho_{\text{air}} \approx 857$). Therefore, the fluid at rest around the flexible structure has a minimal impact on the problem and is neglected for the modal analysis. The meshes consisting of 1926 and 4080 elements were investigated and the results for the first 100 eigenmodes and the corresponding eigenfrequencies do not differ significantly. Therefore, the mesh with 1926 elements is once more sufficient. The results below are based on this grid. In order to understand which kind of deformations occur for a given frequency, the representation of a few selected eigenmodes (EM) is given in Fig. A.28 including their corresponding eigenfrequencies. The first three modes correspond to a simple translation in each Cartesian direction. Then, modes with radial and point-concentrated expansions and contractions (such as EM 4 or 8 and EM 6 or 11) alternate with modes with a dominant deformation in vertical direction (such as EM 10, 22, 56).

A.4. Material modeling

In this appendix the choice of the St. Venant–Kirchhoff material model (Basar and Krätzig, 1985) is justified. This entails the linear elastic isotropic behavior of the herein employed silicone when the corresponding strain is very small (i.e., $\varepsilon^2 \ll \varepsilon$) but the deformations are still large enough that nonlinear strain measures need to be employed (see Basar and Weichert, 2013). For practical applications the latter means that the maximum strain should not exceed about 5%.

For the presented FSI cases, the absolute values of the principal strains ε_1 and ε_2 are computed relying on

$$\varepsilon_1 = \frac{\varepsilon_{11} + \varepsilon_{22}}{2} + \sqrt{\left(\frac{\varepsilon_{11} - \varepsilon_{22}}{2}\right)^2 + \varepsilon_{12}^2}\,, \tag{A.7a}$$

$$\varepsilon_2 = \frac{\varepsilon_{11}+\varepsilon_{22}}{2} - \sqrt{\left(\frac{\varepsilon_{11}-\varepsilon_{22}}{2}\right)^2 + \varepsilon_{12}^2}\,, \tag{A.7b}$$

where ε_{ij} stands for the covariant components of the Green–Lagrange strain tensor defined over the surface of each finite element. Fig. A.29 exemplarily depicts the principal strain contours for the case with significant deformations (i.e., Re = 100,000) at the instance where the maximal values are observed. The maximum of the principal strains is reached on the front side of the hemisphere just before the apex. The investigations show that this maximum does not exceed the limit of 5% for the application of the St. Venant–Kirchhoff material model.

References

Basar, Y., Krätzig, W., 1985. Mechanik der Flächentragwerke. Vieweg, Braunschweig.

Basar, Y., Weichert, D., 2013. Nonlinear Continuum Mechanics of Solids: Fundamental Mathematical and Physical Concepts. Springer Science & Business Media.

Bischoff, M., Bletzinger, K.-U., Wall, W.A., Ramm, E., 2004. Models and finite elements for thin-walled structures. In: Encyclopedia of Computational Mechanics. John Wiley & Sons, Ltd, pp. 1–79.

Bletzinger, K.-U., Wüchner, R., Kupzok, A., 2006. Algorithmic treatment of shells and free form-membranes in FSI. In: Bungartz, H.-J., Schäfer, M. (Eds.), Fluid-Structure Interaction. In: Lecture Notes in Computational Science and Engineering, LNCSE, vol. 53, Springer, Heidelberg, pp. 336–355.

Breitenberger, M., Apostolatos, A., Philipp, B., Wüchner, R., Bletzinger, K.-U., 2015. Analysis in computer aided design: Nonlinear isogeometric B-Rep analysis of shell structures. Comput. Methods Appl. Mech. Engrg. 284, 401–457.

Breuer, M., 2002. Direkte Numerische Simulation und Large-Eddy Simulation turbulenter Strömungen auf Hochleistungsrechnern. In: Habilitationsschrift, Universität Erlangen–Nürnberg, Berichte aus der Strömungstechnik, Shaker Verlag, Aachen, Germany.

Breuer, M., 2018. Effect of inflow turbulence on an airfoil flow with laminar separation bubble: An LES study. Flow Turbul. Combust. https:/doi.org/10.1007/s10494-017-9890-2.

Breuer, M., De Nayer, G., Münsch, M., Gallinger, T., Wüchner, R., 2012. Fluid-structure interaction using a partitioned semi-implicit predictor-corrector coupling scheme for the application of large-eddy simulation. J. Fluids Struct. 29, 107–130.

Causin, P., Gerbeau, J.-F., Nobile, F., 2005. Added-mass effect in the design of partitioned algorithms for fluid-structure problems. Comput. Methods Appl. Mech. Engrg. 194, 42–44.

Chowdhury, I., Dasgupta, S., 2003. Computation of Rayleigh damping coefficients for large systems. Electron. J. Geotech. Eng. 8, 1–11.

de Langre, E., 2002. Fluides et Solides. Éditions École Polytechnique, Paris.

De Nayer, G., Breuer, M., 2014. Numerical FSI investigation based on LES: Flow past a cylinder with a flexible splitter plate involving large deformations (FSI-PfS-2a). Int. J. Heat Fluid Flow 50, 300–315.

De Nayer, G., Kalmbach, A., Breuer, M., Sicklinger, S., Wüchner, R., 2014. Flow past a cylinder with a flexible splitter plate: A complementary experimental-numerical investigation and a new FSI test case (FSI-PfS-1a). Comput. & Fluids 99, 18–43.

De Nayer, G., Schmidt, S., Wood, J.N., Breuer, M., 2018. Enhanced injection method for synthetically generated turbulence within the flow domain of Eddy-resolving simulations. Comput. Math. Appl. 75 (7), 2338–2355.

Durst, F., Schäfer, M., 1996. A parallel block-structured multigrid method for the prediction of incompressible flows. Int. J. Numer. Methods Fluids 22 (6), 549–565.

Farhat, C., van der Zee, K.G., Geuzaine, P., 2006. Provably second-order time-accurate loosely-coupled solution algorithms for transient non-linear computational aeroelasticity. Comput. Methods Appl. Mech. Engrg. 195 (17–18), 1973–2001.

Ferziger, J.H., Perić, M., 2002. Computational Methods for Fluid Dynamics, third ed. Springer Berlin.

Glück, M., Breuer, M., Durst, F., Halfmann, A., Rank, E., 2001. Computation of fluid-structure interaction on lightweight structures. J. Wind Eng. Ind. Aerodyn. 89 (14–15), 1351–1368.

Glück, M., Breuer, M., Durst, F., Halfmann, A., Rank, E., 2003. Computation of wind-induced vibrations of flexible shells and membranous structures. J. Fluids Struct. 17 (5), 739–765.

Hojjat, M., Stavropoulou, E., Gallinger, T., Israel, U., Wüchner, R., Bletzinger, K.-U., 2010. Fluid-structure interaction in the context of shape optimization and computational wind engineering. In: Bungartz, H.-J., Mehl, M., Schäfer, M. (Eds.), Fluid-Structure Interaction II –Modelling, Simulation, Optimization. In: Lecture Notes in Computational Science and Engineering, LNCSE, vol. 73, Springer, Heidelberg, pp. 351–381.

Hughes, T.J., 2012. The finite element method: Linear static and dynamic finite element analysis. Courier Corporation.

Kiendl, J., Schmidt, R., Wüchner, R., Bletzinger, K.-U., 2014. Isogeometric shape optimization of shells using semi-analytical sensitivity analysis and sensitivity weighting. Comput. Methods Appl. Mech. Engrg. 274, 148–167.

Klein, M., Sadiki, A., Janicka, J., 2003. A digital filter based generation of inflow data for spatially–developing direct numerical or large–eddy simulations. J. Comput. Phys. 186, 652–665.

Kupzok, A.M., 2009. Modeling the Interaction of Wind and Membrane Structures by Numerical Simulation (Ph.D. thesis), Lehrstuhl für Statik, Technische Universität München, Germany.

Michalski, A., Gawenat, B., Gelenne, P., Haug, E., 2015. Computational wind engineering of large umbrella structures. J. Wind Eng. Ind. Aerodyn. 144, 96–107.

Michalski, A., Kermel, P., Haug, E., Löhner, R., Wüchner, R., Bletzinger, K.-U., 2011. Validation of the computational fluid–structure interaction simulation at real-scale tests of a flexible 29 m umbrella in natural wind flow. J. Wind Eng. Ind. Aerodyn. 99 (4), 400–413.

Philipp, B., Breitenberger, M., Wüchner, R., Bletzinger, K.-U., 2015. Form-finding of architectural membranes in a CAD-environment using the AiCAD-concept. In: Ramsgaard Thomsen, M., Tamke, M., Gengnagel, C., Faircloth, B., Scheurer, F. (Eds.), Modelling Behaviour. Springer, pp. 65–74.

Piomelli, U., Chasnov, J.R., 1996. Large–eddy simulations: Theory and Applications. In: Hallbäck, M., Henningson, D., Johansson, A., Alfredson, P. (Eds.), Turbulence and Transition Modeling. Kluwer, pp. 269–331.

Rank, E., Halfmann, A., Glück, M., Breuer, M., Durst, F., Kaiser, U., Bergmann, D., Wagner, S., 2003. Windbelastung leichter Flächentragwerke: Numerische Simulation und Windkanalversuch. Bauingenieur 501–508.

Rossi, R., 2013. Advanced methods for the coupled simulation of membrane systems: Towards a virtual wind tunnel, in: VI International Conference on Textile Composites and Inflatable Structures, Structural Membranes, Munich, Germany.

Schmidt, S., Breuer, M., 2014. Hybrid LES–URANS Methodology for the prediction of non–equilibrium wall–bounded internal and external flows. Comput. & Fluids 96, 226–252.

Schmidt, S., Breuer, M., 2017. Source term based synthetic turbulence inflow generator for Eddy–Resolving predictions of an airfoil flow including a laminar separation bubble. Comput. & Fluids 146, 1–22.

Schweizerhof, K., Ramm, E., 1984. Displacement dependent pressure loads in nonlinear finite element analyses. Comput. Struct. 18 (6), 1099–1114.

Sen, S., De Nayer, G., Breuer, M., 2017. A fast and robust hybrid method for block-structured mesh adaption with emphasis on FSI-LES applications. Int. J. Numer. Methods Engrg. 111 (3), 273–300.
Sicklinger, S., Belsky, V., Engelmann, B., Elmqvist, H., Olsson, H., Wüchner, R., Bletzinger, K.-U., 2014. Interface Jacobian-based co-simulation. Int. J. Numer. Methods Engrg. 98 (6), 418–444.
Smagorinsky, J., 1963. General circulation experiments with the primitive equations I: The basic experiment. Mon. Weather Rev. 91 (3), 99–165.
Thompson, J.F., Warsi, Z.U.A., Wayne Mastin, C., 1985. Numerical Grid Generation: Foundations and Applications, vol. 45. North-Holland.
Wang, T., Wüchner, R., Sicklinger, S., Bletzinger, K.-U., 2016. Assessment and improvement of mapping algorithms for non-matching meshes and geometries in computational FSI. Comput. Mech. 57 (5), 793–816.
Wood, J.N., Breuer, M., De Nayer, G., 2018. Experimental studies on the fluid-structure interaction of an air-inflated flexible hemisphere in turbulent flows. J. Fluids Struct. 80, 405–440.
Wood, J.N., De Nayer, G., Schmidt, S., Breuer, M., 2016. Experimental investigation and large-eddy simulation of the turbulent flow past a smooth and rigid hemisphere. Flow Turbul. Combust. 97 (1), 79–119.
Wüchner, R., Bletzinger, K.-U., 2005. Stress-adapted numerical form finding of pre-stressed surfaces by the updated reference strategy. Int. J. Numer. Methods Engrg. 64 (2), 143–166.
Wüchner, R., Kupzok, A., Bletzinger, K.-U., 2007. A framework for stabilized partitioned analysis of thin membrane-wind interaction. Int. J. Numer. Methods Fluids 54 (6–8), 945–963.